OBJECTIVE: **The Tsunami Society** publishes this journal to increase and disseminate knowledge about tsunamis and their hazards.

DISCLAIMER: Although these articles have been technically reviewed by peers, **The Tsunami Society** is not responsible for the veracity of any statement, opinion or consequences.

EDITORIAL STAFF

Dr. Charles Mader, Editor
  Mader Consulting Co.
  1049 Kamehame Dr., Honolulu, HI. 96825-2860, USA

Dr. Augustine Furumoto, Publisher

EDITORIAL BOARD

Dr. Antonio Baptista, Oregon Graduate Institute of Science and Technology
Professor George Carrier, Harvard University
Mr. George Curtis, University of Hawaii - Hilo
Dr. Zygmunt Kowalik, University of Alaska
Dr. Shigehisa Nakamura, Kyoto University
Dr. Yurii Shokin, Novosibirsk
Mr. Thomas Sokolowski, Alaska Tsunami Warning Center
Dr. Costas Synolakis, University of California
Professor Stefano Tinti, University of Bologna

TSUNAMI SOCIETY OFFICERS

Mr. George Curtis, President
Professor Stefano Tinti, Vice President
Dr. Charles McCreery, Secretary
Dr. Augustine Furumoto, Treasurer

Submit manuscripts of articles, notes or letters to the Editor. If an article is accepted for publication the author(s) must submit a camera ready manuscript in the journal format. A voluntary $50.00 page charge ($35.00 for Tsunami Society Members) will include 50 reprints.

SUBSCRIPTION INFORMATION: Price per copy $20.00 USA

PREDICTING TSUNAMI AMPLITUDES ALONG THE NORTH AMERICAN COAST FROM TSUNAMIS GENERATED IN THE NORTHWEST PACIFIC OCEAN DURING TSUNAMI WARNINGS

Paul M. Whitmore and Thomas J. Sokolowski
NOAA/National Weather Service
Alaska Tsunami Warning Center
910 South Felton Street
Palmer, Alaska 99645

ABSTRACT

This study describes a beginning method to provide emergency managers along the Pacific coasts of Alaska, British Columbia, Washington, Oregon, and California a reasonable range of expected wave heights during a tsunami warning for tsunamis generated in the northwest Pacific Ocean. Expected amplitudes at 80 sites for 15 hypothetical earthquakes in the northwest Pacific ranging from Mw 7.5 to Mw 9.0 are shown. Historic tsunamis generated in the subduction zone east of northern Honshu, the Kuril Islands, and Kamchatka are modeled using the shallow water equations to validate this approach. These simulations show that tsunami amplitudes near the North American coast can be predicted prior to impact given the earthquake's moment magnitude and two or more tide gage readings outside the source zone which are used to calibrate the pre-computed models. One method of distributing these results would be to release them as a range of expected values which take into account uncertainties in the method. As more accurate modeling techniques and water level data become available, they can be used to improve this method.

148

INTRODUCTION

Presently, tsunami warnings in the United States and Canada are issued giving the recipients information- such as earthquake location and magnitude, tsunami arrival time, warning boundaries, and general information on tsunamis. No information is provided on the expected wave height. The October 4, 1994 Kuril Islands tsunami and subsequent Pacific-wide warning, in which many facilities along the U.S. coast were needlessly evacuated, highlighted the demand for a reasonable estimate of expected tsunami amplitude in addition to the arrival time.

An approach is described here to provide emergency officials in Alaska, British Columbia, Washington, Oregon, and California, which is the Alaska Tsunami Warning Center area of responsibility or ATWC AOR, a range of expected tsunami wave heights near the coast for earthquakes which occur along the trench from northern Honshu, Japan to the Commander Islands, Russia (the study area). The estimates will only be made after the tsunami has been recorded on two or more tide gages away from the source zone. Data from tide gages near the source are not considered reliable due to large amplifications of the wave that often occur near the source. Tide gage data at locations such as Midway Island, Shemya, or Adak, Alaska can be used to calibrate pre-computed models in time to give officials in the ATWC AOR useful information on expected tsunami size. This approach is a first step in the estimation of tsunami amplitudes during tsunami warnings. Future enhancements to the technique can be added to improve accuracy.

To predict tsunami amplitudes, a series of models for hypothetical earthquakes in the study area are generated using a technique described by Kowalik and Whitmore (1991). The study area is divided into the following subsets: northern Honshu, southern Kuril Islands, northern Kuril Islands/southern Kamchatka, Kamchatka, and the Commander Islands. Three models are computed in each subset for earthquakes of moment magnitudes 7.5, 8.2, and 9.0. Tsunami amplitudes at 80 sites along the North American coast and Midway Island are saved in each model. Historic earthquakes in each zone are also modeled and compared with actual tide gage amplitudes to determine uncertainty in the results. During a tsunami warning, the results from the most appropriate model (based on location and moment magnitude) will be scaled by a factor determined from the observed amplitude at tide gages such as those listed above and the modeled amplitude at those tide gages. The scale factor is applied to pre-computed amplitudes to give the expected amplitude at 80 locations along the coast from the western Aleutian Islands through southern California. Model uncertainty and a safety factor are taken into account and a range of expected wave heights could then be provided to the emergency officials.

This method can also be extended to other areas of the Pacific Ocean which are potentially dangerous to the ATWC AOR outside of the source zone. Figure 1 displays locations of earthquakes which have produced recorded tsunami amplitudes or runups greater than 25cm outside the source zone and within the ATWC AOR (Lander and Lockridge, 1989, Lander et al., 1993). These figures show that the areas of concern are Chile, Alaska, Hawaii, and the area of this study.

MODELING TECHNIQUE

Tsunami generation is accomplished by uplift of the sea-floor during an earthquake. Okada's (1985) static dislocation formulae are used to compute the amount of vertical uplift given the earthquake's strike, dip, slip, length, width, depth, moment, location, and Lame's constants for the surrounding rocks. The sea-floor is instantaneously uplifted at the beginning of the computations. The shallow water equations of motion and the continuity equation solved over

a spherical grid (Kowalik and Murty, 1993) are then used to propagate the tsunami across the ocean to the North American coast. These equations are:

$$\frac{\partial u}{\partial t} + u\frac{\partial u}{R\cos\varphi\,\partial\lambda} + v\frac{\partial u}{R\partial\varphi} = \frac{-g}{R\cos\varphi}\frac{\partial\zeta}{\partial\lambda} - \frac{ru(u^2+v^2)^{1/2}}{(\zeta+H-\eta)}$$ (1)

$$\frac{\partial v}{\partial t} + u\frac{\partial v}{R\cos\varphi\,\partial\lambda} + v\frac{\partial v}{R\partial\varphi} = \frac{-g}{R}\frac{\partial\zeta}{\partial\varphi} - \frac{rv(u^2+v^2)^{1/2}}{(\zeta+H-\eta)}$$ (2)

$$\frac{1}{R\cos\varphi}\left(\frac{\partial(u(\zeta+H-\eta))}{\partial\lambda} + \frac{\partial(v(\zeta+H-\eta))\cos\varphi}{\partial\varphi}\right) = \frac{\partial\eta}{\partial t} - \frac{\partial\zeta}{\partial t},$$ (3)

where: u is the east-west particle velocity, v is the north-south particle velocity, ζ denotes the variation of sea-level from equilibrium, t is time, g is gravitational acceleration (g=9.81m/s^2), R is the earth radius (R=6370km), φ is latitude, λ is longitude, η is bottom displacement, r is the coefficient of bottom friction, and H is water depth prior to source displacement. The bottom friction coefficient, r, is set to 0.005 over the continental shelf and 0.01 in the near shore shallow water as in Aida (1983). The coriolis term along with bottom friction and non-linear terms in coarse grid computations are omitted based on testing by Kowalik and Whitmore (1991).

Equations 1 through 3 are solved by a finite difference technique discussed in detail in Kowalik and Whitmore (1991). The technique allows for fine grids within the overall coarse grid and for very-fine grids within the fine grids. The grids dynamically interact. That is, actions within the fine grids affect computations within the coarse grid. Sea-levels and velocities are computed at every time step for points in all grids, though CPU time is saved by not starting computations within a fine or very-fine grid until the tsunami has arrived. A version of NOAA's ETOPO5 grid which has been edited near the North American coast is used for the north Pacific-wide coarse grid. This grid has a 5 minute spacing. The fine grids have a 1 minute grid point spacing. These were designed so that there are 10 to 20 grid points per tsunami wavelength over the continental shelf as was shown necessary by Shuto et al. (1985). With a 1 minute increment, wave amplitudes for the listed sites in fine grids are modeled between 500m and 900m offshore. This distance takes into account that wave heights are computed between velocity points, and smaller east-west spacing with increasing latitude. Coastal areas with complex bathymetries or shoreline configuration were gridded with a very-fine grid inside of the fine grid. The grid point spacing within the very-fine grids range from 6.6 seconds to 12 seconds. In the very-fine grids modeled amplitudes for the listed sites are between 100m and 200m offshore. Fine and very-fine grid bathymetric data were edited with NOS hydrographic maps. In total, 56 sub-grids were set-up along the North American coast and Midway Island.

The open ocean and coastline boundary conditions are determined as follows. Velocities are set to 0 at the coastline. No inundation effects are taken into account. At the open ocean boundaries the radiation conditions from Reid and Bodine (1968),

$$u = \pm(\zeta(\frac{g}{H})^{1/2})\ and$$
$$v = \pm(\zeta(\frac{g}{H})^{1/2}),$$ (4)

are used.

The models are computed for 7 hours after the tsunami arrives at the fine grids. For example, the total model run time for a tsunami generated in the Kuril Islands to the U.S. west coast is about 15 hours. The models are performed on a 90 MHz Pentium PC running the OS/2 operating system. Due to memory limitations, each model is performed in four sections. The tsunami is first propagated from the source into the California fine and very-fine grids. Then the model is repeated from the source to the grids in Oregon, Washington, and British Columbia. Then again to the grids in south Alaska and lastly to the Aleutian Islands. Breaking the models up in this manner preserves the dynamic interaction between grids of different spacing, though it is time consuming. A complete model for each hypothetical earthquake takes about 8 days to complete.

COMPARISON TO HISTORIC TSUNAMIS

The modeling technique's validity is tested by comparing modeled results with five of the largest tsunamis generated in the study area. The only recorded tsunami generated in the study area which produced a sizeable tsunami in the ATWC AOR which is not modeled here is the 1896 Sanriku tsunami. Maximum observed wave amplitudes in this event were 1.5m at Santa Cruz and 1.0m at Mendocino (Lander et al., 1993). This tsunami could not be modeled as there is no reliable information on the earthquake source.

Table 1 lists the source parameters for the five simulated earthquakes. Figures 2 through 4 compare modeled versus recorded tsunami amplitudes for the 1952, 1968, and 1994 tsunamis. Table 2 lists the comparison for the 1958 and 1963 tsunamis which were not recorded on many tide gages. The amplitudes given are zero-to-peak in meters. The results show that the modeled amplitudes represent the recorded data reasonably well. Considering recorded tsunamis over 20cm, the modeled amplitudes have an average error of 36% compared to the recorded data and a maximum error of 127%. The largest percentage errors occur in the smaller tsunamis. For the larger tsunamis (those over 1m amplitude), the modeled results were all within 26%.

Many approximations are used in this modeling technique and are partly responsible for the differences between modeled and recorded tsunamis. The tsunami source is greatly simplified by assuming a rectangular fault plane with constant slip. The actual fault planes and slip distributions are more complex. No secondary source effects such as co-seismic landslides or slip along secondary faults are taken into account. Simplifications used in the wave propagation also may influence the modeled tsunamis. The shallow water approximation utilized here does not include dispersive terms which may be important in trans-Pacific models (Mader et al., 1993). Addition of the friction coefficient and coriolis term to the equations of motion in the coarse grid may also have a small effect. Accounting for inundation along shorelines will also influence what is modeled at the tide gage locations. Lastly, it is well known that a tsunami signal recorded on a tide gage does not exactly represent the tsunami (e.g. Satake, 1987). They are the only records, though, available to test this technique.

Figure 5 compares recorded tide gage data to the modeled signal for the 1952 Kamchatka tsunami. The 1952 event was the largest tsunami recorded in the ATWC AOR generated in the study area. Figure 5 shows that the character of the first few tsunami cycles is represented reasonably well at most locations. The character difference at the Midway Island tide gage, though, is very distinct even though the amplitude is within 30% This character difference at Midway Island held true for all the models.

The 1994 tsunami was generated by an oblique-slip earthquake which has two very different proposed fault planes. Results in Figure 4 are generated using the proposed fault plane of Kikuchi and Kanamori (1995) which follows the trend of the trench. Tanioka et al. (1995) proposed that the fault strike is perpendicular to the trench. To determine the importance of

fault plane orientation for this study, both sets of source parameters were used as input to the modeling program. The distribution of recorded tsunami amplitudes along the ATWC AOR can be explained by either model. This observation is encouraging in that knowledge of the exact fault parameters, at least for earthquakes of this magnitude and fault length, does not appear necessary to produce a reasonable estimate of the expected tsunami wave heights in the ATWC AOR.

POSSIBLE MODEL APPLICATION TO FUTURE WARNINGS

Fifteen hypothetical earthquakes in the study area are modeled and amplitudes recorded at 80 sites along the North American coast and Midway Island. Source parameters for these hypothetical earthquakes are listed in Table 3. Parameters are based on historic earthquakes in the sub-area, strike of the subduction zone, and magnitude/fault area relationships given in Kanamori and Anderson (1975). No large, historic earthquakes have occurred in the Commander Islands section of the Aleutian subduction zone so a predominantly right-lateral, strike-slip fault was chosen based on present plate motions (Engebretson et al., 1985). The study area is divided into five sub-areas: northern Honshu, southern Kuril Islands, northern Kuril Islands/southern Kamchatka, Kamchatka, and the Commander Islands. Moment magnitude 7.5, 8.2, and 9.0 earthquakes are simulated in each sub-area. Results from the 15 simulations are shown in Figures 6 through 10.

One way to utilize these models during future warnings for tsunamis generated in the study area is as follows. Results from the modeled earthquake which best match the size and location of the earthquake which triggered the tsunami warning are selected. This set of expected amplitudes is then multiplied by a scale factor determined from the observed amplitudes at the first two tide gages which record the tsunami. This scaling factor (SF) is figured in a simple manner.

$$ SF = \frac{\sum_{i=1}^{N} \frac{REC\,(i)}{MOD\,(i)}}{N}, \qquad\qquad (5) $$

where MOD is the modeled amplitude at tide gage i, REC is the recorded amplitude at tide gage i, and N is the number of tide gages averaged. The selected set of pre-computed amplitudes are multiplied by the scaling factor and released as an expected range of tsunami wave heights at the locations listed in Figures 6 through 10. As the tsunami travels across the ocean, more tide gage data can be added in equation 5 to refine the predictions. The scaled amplitude is converted to a range, in peak-to-trough wave height, based on the uncertainty of the method and adding a safety factor of approximately 40% based on the historic models. Results are output as wave heights instead of amplitudes as emergency officials are more familiar with this measurement. If, during a tsunami warning, the recorded tide gage data are much greater than expected from the pre-computed modeling and the predicted values are in doubt, the duty geophysicist can issue a warning with no expected wave heights.

Uncertainty in this method can be determined by examining the five tsunamis listed in the previous section along with the 1952 Hokkaido tsunami. Each historic tsunami is treated as an event for which a tsunami warning has just been issued. The most appropriate set of pre-computed amplitudes is chosen based on the earthquake's location and moment magnitude. These pre-computed amplitudes are multiplied by the scaling factor computed from two recorded tsunamis at Midway Island, Attu, Shemya, or Adak (Table 4). Table 5 lists the

amplitudes which would have been predicted for the six tsunamis along with the recorded amplitudes. Considering the comparison in Table 5 and a safety factor of at least 40%, predicted values are converted to wave height ranges as listed in Table 6. There is no way to figure the technique's uncertainty for predicted values over 2.0m given the historical data. For now, if predicted amplitudes are over 2.0m, a warning will be issued with no wave height estimates. When this technique is extended for Alaskan earthquakes, uncertainty for larger tsunamis can be determined and utilized for northwest Pacific source zone.

CONCLUSIONS

Pre-computed tsunami models for hypothetical earthquakes along the trench from northern Honshu, Japan to the Commander Islands, Russia can be used in conjunction with observed tide gage data to give emergency managers in the ATWC AOR a reasonable tsunami wave height estimate during tsunami warnings. A scale factor, determined from the observed tide gage amplitudes to the expected amplitude, is applied to the pre-computed amplitudes. Results are then disseminated to officials along the coast as a range of possible wave heights which take into account uncertainty in the method.

As there are a limited number of events in the study area which produced tsunamis in the ATWC AOR, three of these (1952 Kamchatka, 1968 Honshu, and 1994 Kuril Islands) were used for both determining likely source parameters of future events and for determining the uncertainty of the method. The uncertainty was also checked by using three events which were not used in the hypothetical tsunami models (1958 Kuril Islands, 1963 Kuril Islands, and 1952 Hokkaido). Table 5 shows that these three events would have predicted amplitudes with similar accuracy as the first three events. Predicted amplitudes from the southern Kuril Islands sub-area were checked with both the 1994 oblique-slip event and the 1963 dip-slip event. Both predictions would have given reasonable results, if made during the events, even though they were based on a pre-computed model with oblique-slip fault motion.

Real-time signal from proposed deep-water tide gages (Gonzalez and Milburn, 1995) would give another means of checking or scaling the pre-computed amplitudes during a warning. If placed appropriately, deep-water gages also could extend this technique to Hawaii for tsunamis generated in the northwest Pacific.

The technique described in this report must be viewed as a starting point at tsunami amplitude estimation during tsunami warnings in the ATWC AOR. As the technique is used and extended to other source areas of the Pacific, refinements can be added or procedures changed as necessary. Future modeling performed on faster computers can eliminate some of the potential sources of error in the wave propagation formulas.

ACKNOWLEDGMENTS

References

Aida, I.: 1983, Numerical simulation of historical tsunamis generated off the Tokai district in central Japan, in K. Iida and T. Iwasaki (eds.), *Tsunamis - Their Science and Engineering*, TERRAPUB, Tokyo, Japan, 277-291.

Beck, S. and Ruff, L.J.: 1987, Rupture process of the great 1963 Kuril Islands earthquake sequence: asperity interaction and multiple event rupture, *J. Geophys. Res.*, 92, 14123-14138.

Engebretson, D.C., Cox, A., and Gordon, R.G.: 1985, *Relative Motions between Oceanic and Continental Plates in the Pacific Basin*, GSA Special Paper 206, 59 pp.

Fukao, Y. and Furumoto, M.: 1979, Stress drops, wave spectra, and recurrence intervals of great earthquakes - implications of the Etorofu earthquake of 1958 November 6, *Geophys. J. R. Astr. Soc.*, 57, 23-40.

Gonzalez, F.I. and Milburn, H.B.:1995, Near-source tsunami measurements for forecast and warning, in M. Blackford and H. Kanamori, *Tsunami Warning System Workshop Report*, NOAA Tech. Mem. ERL PMEL-105, pp. 75-78.

Kanamori, H.: 1970, Synthesis of long-period surface waves and its application to earthquake source studies - Kuril Islands earthquake of October 13, 1963, *J. Geophys. Res.*, 75, 5011-5027.

Kanamori, H.: 1971, Focal mechanism of the Tokachi-Oki earthquake of May 16, 1968: contortion of the lithosphere at the junction of two trenches, *Tectonophysics*, 12, 1-13.

Kanamori, H.: 1976, Re-examination of the earth's free oscillations excited by the Kamchatka earthquake of November 4, 1952, *Phys. Earth Planet. Int.*, 11, 216-226.

Kanamori, H. and Anderson, D.L.: 1975, Theoretical basis of some empirical relations in seismology, *Bull. Seism. Soc. Am.* 65, 1073-1095.

Kikuchi, M. and Fukao, Y.: 1985, Iterative deconvolution of complex body waves from great earthquakes - the Tokachi-Oki earthquake of 1968, *Phys. Earth Planet. Int.*, 37, 235-248.

Kikuchi, M. and Kanamori, H.: 1995, The Shikotan earthquake of October 4, 1994: Lithospheric earthquake, *Geophysical Research Letters*, 22, 1025-1028.

Kowalik, Z. and Whitmore, P.M.: 1991, An investigation of two tsunamis recorded at Adak, Alaska, *Sci. Tsunami Hazards* 9, 67-83.

Kowalik, Z. and Murty, T.S.: 1993, *Numerical Modeling of Ocean Dynamics*, World Scientific, Singapore, pp. 5-19.

Lander, J.F. and Lockridge, P.A.: 1989, *United States Tsunamis (including United States possessions) 1690-1988*, NOAA Pub. 41-2, pp. 166-169.

Lander, J.F., Lockridge, P.A., and Kozuch, M.J.: 1993, *Tsunamis Affecting the West Coast of the United States 1806-1992*, NGDC Key to Geophysical Records Doc. #29, pp. 120-150.

Mader, C.L., Moore, D.W., and Carrier, G.F.: 1993, Numerical tsunami propagation study - III, *Sci. Tsunami Haz.*, 11, 93-107.

Okada, Y.: 1985, Surface deformation due to shear and tensile faults in a half-space, *Bull. Seism. Soc. Am.* 75, 1135-1154.

Reid, R.O. and Bodine, B.R.: 1968, Numerical model for storm surges in Galveston Bay, *J. Waterway Harbor Div.* 94(WW1), 33-57.

Satake, K.: 1987, Inversion of tsunami waveforms for the estimation of a fault heterogeneity: Method and numerical experiments, *J. Phys. Earth*, 35, 241-254.

Satake, K.: 1989, Inversion of tsunami waveforms for the estimation of heterogenous fault motion of large submarine earthquakes: the 1968 Tokachi-Oki and 1983 Japan Sea earthquakes, *J. Geophys. Res.*, 94, 5627-5636.

Shuto, N., Suzuki, T., Hasegawa, K., and Inagaki, K.: 1985, Summary of a study of numerical technique on the tsunami propagation and runup, in T.S. Murty and W.J. Rapatz (eds.), *Proc. Int. Tsunami Symp.*, Inst. Ocean Sci., Sidney, B.C., Canada, 88-92.

Tanioka, Y., Ruff, L., and Satake, K.: 1995, The great Kurile earthquake of October 4, 1994 tore the slab, *Geophysical Research Letters*, 22, 1661-1664.

U.S. Dept. of Commerce: 1953, *The Tsunami of November 4, 1952 as Recorded at Tide Stations*, Special Publication # 300, U.S. GPO, Washington D.C., 24-46.

Table I. Source Parameters of Historic Earthquakes

Date	Location Lat. Lon.		Strike (°)	Dip (°)	Slip (°)	Length (km)	Width (km)	Depth (km)	Mw	Ref.
11-4-52	53.2N	158.5E	214	30	110	650	200	103	9.0	1
11-6-58	44.4N	148.6E	225	30	90	150	70	53	8.4	2
10-13-63	44.8N	149.5E	223	22	90	245	150	59	8.6	3,4
5-16-68	41.5N	142.0E	156	20	38	200	100	43	8.2	5,6,7
10-4-94	42.5N	146.1E	54	76	129	185	70	85	8.2	8,9

Note: Depth refers to bottom depth of the fault plane. Location is a point on the fault plane.
References: 1 - Kanamori (1976); 2 - Fukao and Furumoto (1979); 3 - Kanamori (1970); 4 - Beck and Ruff (1987); 5 - Kanamori (1971); 6 - Satake (1989); 7 - Kikuchi and Fukao (1985); 8 - Kikuchi and Kanamori (1995); 9 - Japan Meteorological Agency aftershock locations.

Table II. Modeled Versus Recorded Tsunami Amplitudes

Location	1958 tsunami		1963 tsunami	
	Recorded	Modeled	Recorded	Modeled
Attu, AK	0.2	0.62	0.4	0.63
Adak, AK	0.1	0.38		
Crescent City, CA			0.5	0.41
San Francisco, CA	0.2	0.12	<0.1	0.11
Avila, CA	0.15	0.48	0.3	0.40
Los Angeles, CA			<0.1	0.15
La Jolla, CA			0.1	0.28
Midway I., HI	0.2	0.52	0.3	0.54

Note: Values listed are zero-to-peak tsunami amplitude in meters. Recorded data from Lander and Lockridge (1989) and Lander *et al.* (1993).

Table III. Source Parameters of Hypothetical Earthquakes

Area	Location Lat. Lon.	Strike (°)	Dip (°)	Slip (°)	Length (km)	Width (km)	Depth (km)	Mw
Northern	39.5N 143.6E	182	20	90	60	37	18	7.5
Honshu	41.5N 142.0E	156	20	38	200	100	43	8.2
	41.3N 141.8E	182	20	90	650	200	73	9.0
S. Kuril	43.3N 147.5E	54	76	129	70	30	44	7.5
Islands	42.5N 146.1E	54	76	129	185	70	84	8.2
	41.7N 144.6E	54	76	129	900	130	141	9.0
N. Kuril/	52.7N 160.6E	214	30	90	60	37	21	7.5
S. Kamchatka	52.7N 160.2E	214	30	90	200	70	38	8.2
	53.2N 158.5E	214	30	110	650	200	103	9.0
Kamchatka	56.1N 164.0E	214	30	90	60	37	21	7.5
	56.2N 163.6E	214	30	90	200	70	38	8.2
	56.6N 162.0E	214	30	90	650	200	103	9.0
Commander	54.2N 167.5E	300	30	160	70	30	35	7.5
Islands	53.6N 169.0E	300	30	160	200	65	69	8.2
	52.2N 174.0E	300	30	160	800	100	104	9.0

Note: Depth refers to bottom depth of the fault plane. Location is the down-dip inner corner (with respect to the strike vector) of the fault plane.

Table IV. Scale Factor Computation

Tsunami	Tide gage	Amplitudes	Scale Factor
1952 Hokkaido	Attu Adak	0.3/0.30 0.1/0.25	0.70
1952 Kamchatka	Adak Midway	1.3/0.96 1.28/0.98	1.33
1958 S. Kuril	Attu Midway	0.2/0.21 0.2/0.36	0.75
1963 S. Kuril	Attu Midway	0.4/0.21 0.3/0.36	1.37
1968 N. Honshu	Attu Midway	0.2/0.30 0.2/0.33	0.64
1994 S. Kuril	Shemya Midway	0.15/0.20 0.27/0.36	0.75

Note: Listed tsunamis are *recorded/predicted.* These are zero-to-peak amplitude in meters.

Table V. Uncertainty Test Results

Location	1952 Hokkaido	1952 Kamchatka	1958 S. Kuril	1963 S. Kuril	1968 N. Honshu	1994 S. Kuril
Adak			<0.1/0.12		<0.1/0.16	0.15/0.12
Dutch Harbor	0.1/0.04	0.6/0.82			<0.1/0.04	0.08/0.03
Kodiak		0.2/0.52				
Seward		0.1/0.25				
Yakutat		0.3/0.42				
Sitka	0.1/0.07	0.3/0.89			<0.1/0.06	0.04/0.16
Tofino		0.3/0.90				
Neah Bay		0.2/0.42			<0.1/0.06	0.04/0.05
Seattle		<0.1/0.13				
Port Angeles						0.06/0.02
Astoria		0.1/0.17				
Newport					0.2/0.12	0.05/0.19
Charleston						0.09/0.15
Port Orford						0.18/0.34
Crescent City	0.2/0.22	1.0/1.53		0.5/0.60	0.6/0.20	0.50/0.33
Humboldt Bay						0.10/0.19
Arena Cove						0.14/0.20
San Francisco	<0.1/0.06	0.6/0.72	0.2/0.07	<0.1/0.12	<0.1/0.05	
Alameda	<0.1/0.03	0.4/0.43			<0.1/0.03	0.04/0.04
Sausalito	<0.1/0.04					
Avila		1.4/1.68	0.15/0.14	0.3/0.26	<0.1/0.08	
Port San Luis						0.15/0.14
Santa Barbara						0.08/0.04
Santa Monica		0.5/0.89			0.2/0.06	0.09/0.09
Los Angeles	0.1/0.05	0.3/0.49		<0.1/0.16	<0.1/0.04	0.06/0.09
Newport					<0.1/0.04	
La Jolla	<0.1/0.08	0.2/0.70		0.1/0.30	<0.1/0.07	0.03/0.17
San Diego	<0.1/0.08	0.3/0.40			<0.1/0.07	

Note: Listed values are *recorded amplitude/hindcast amplitude*. These are zero-to-peak tsunami amplitude in meters.

Table VI. Output Ranges

Predicted Amps.	Output Range
0.00 - 0.15	Up to 0.6m
0.15 - 0.30	Up to 1.2m
0.30 - 0.60	Up to 1.7m
0.60 - 0.90	Up to 2.5m
0.90 - 1.20	Up to 3.4m
1.20 - 1.60	Up to 4.5m
1.60 - 2.00	Up to 5.6m

Note: Predicted amplitudes listed are zero-to-peak in meters. Any predicted amplitude within the given interval would be output as the listed range. The output range is peak-to-trough wave height in meters.
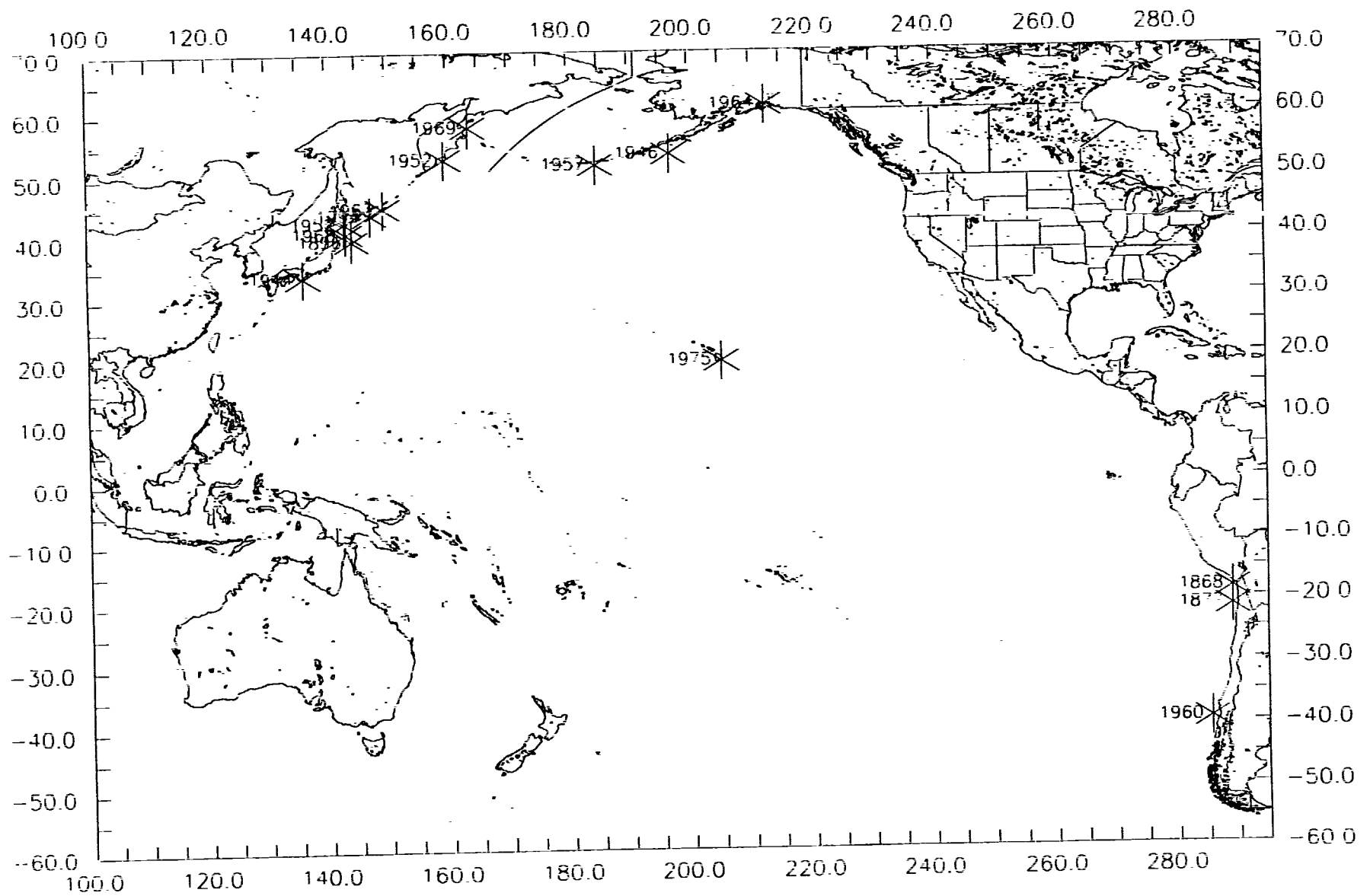
Figure 1.)   Location of tsunami generating earthquakes which produced tsunamis greater than 25cm amplitude within the ATWC AOR and outside the source zone.
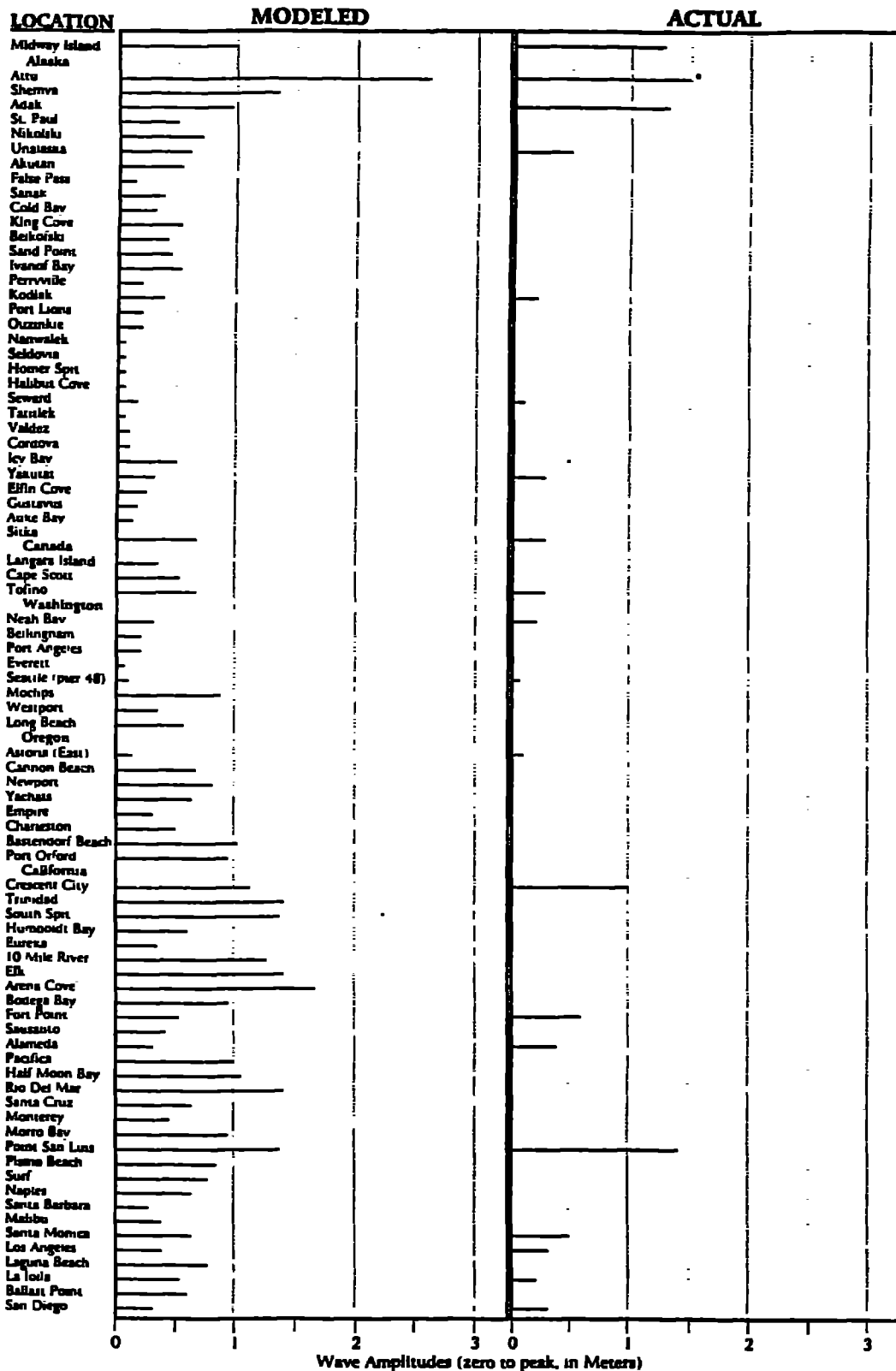
LOCATION MODELED ACTUAL

Midway Island
Alaska
Attu
Shemya
Adak
St. Paul
Nikolski
Unalaska
Akutan
False Pass
Sanak
Cold Bay
King Cove
Belkofski
Sand Point
Ivanof Bay
Perryville
Kodiak
Port Lions
Ouzinkie
Nanwalek
Seldovia
Homer Spit
Halibut Cove
Seward
Tarniek
Valdez
Cordova
Icy Bay
Yakutat
Elfin Cove
Gustavus
Auke Bay
Sitka
Canada
Langara Island
Cape Scott
Tofino
Washington
Neah Bay
Bellingham
Port Angeles
Everett
Seattle (pier 48)
Mochips
Westport
Long Beach
Oregon
Astoria (East)
Cannon Beach
Newport
Yachats
Empire
Charleston
Bastendorf Beach
Port Orford
California
Crescent City
Trinidad
South Spit
Humboldt Bay
Eureka
10 Mile River
Elk
Arena Cove
Bodega Bay
Fort Point
Sausalito
Alameda
Pacifica
Half Moon Bay
Rio Del Mar
Santa Cruz
Monterey
Morro Bay
Point San Luis
Pismo Beach
Surf
Naples
Santa Barbara
Malibu
Santa Monica
Los Angeles
Laguna Beach
La Jolla
Ballast Point
San Diego

0   1   2   3   0   1   2   3

Wave Amplitudes (zero to peak, in Meters)

Figure 2.)   Comparison of recorded versus modeled amplitudes for the November 4, 1952 Kamchatka earthquake and tsunami. Amplitudes listed are zero-to-peak in meters. All tide gages which recorded a tsunami and had a model performed at that location a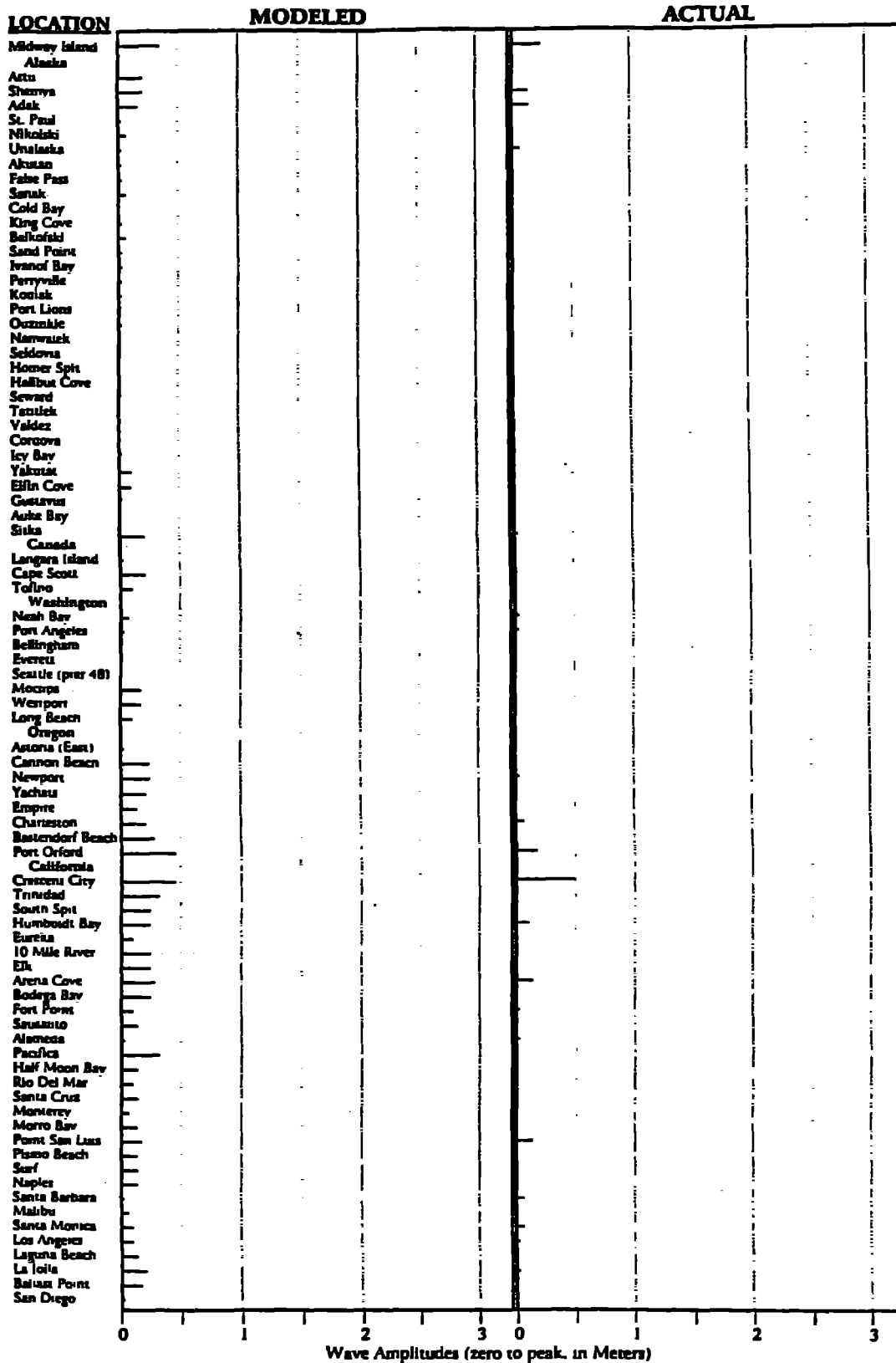re shown along with the other modeled amplitudes. At Attu, the * indicates the tide gage was inoperable during the largest part of the tsunami.
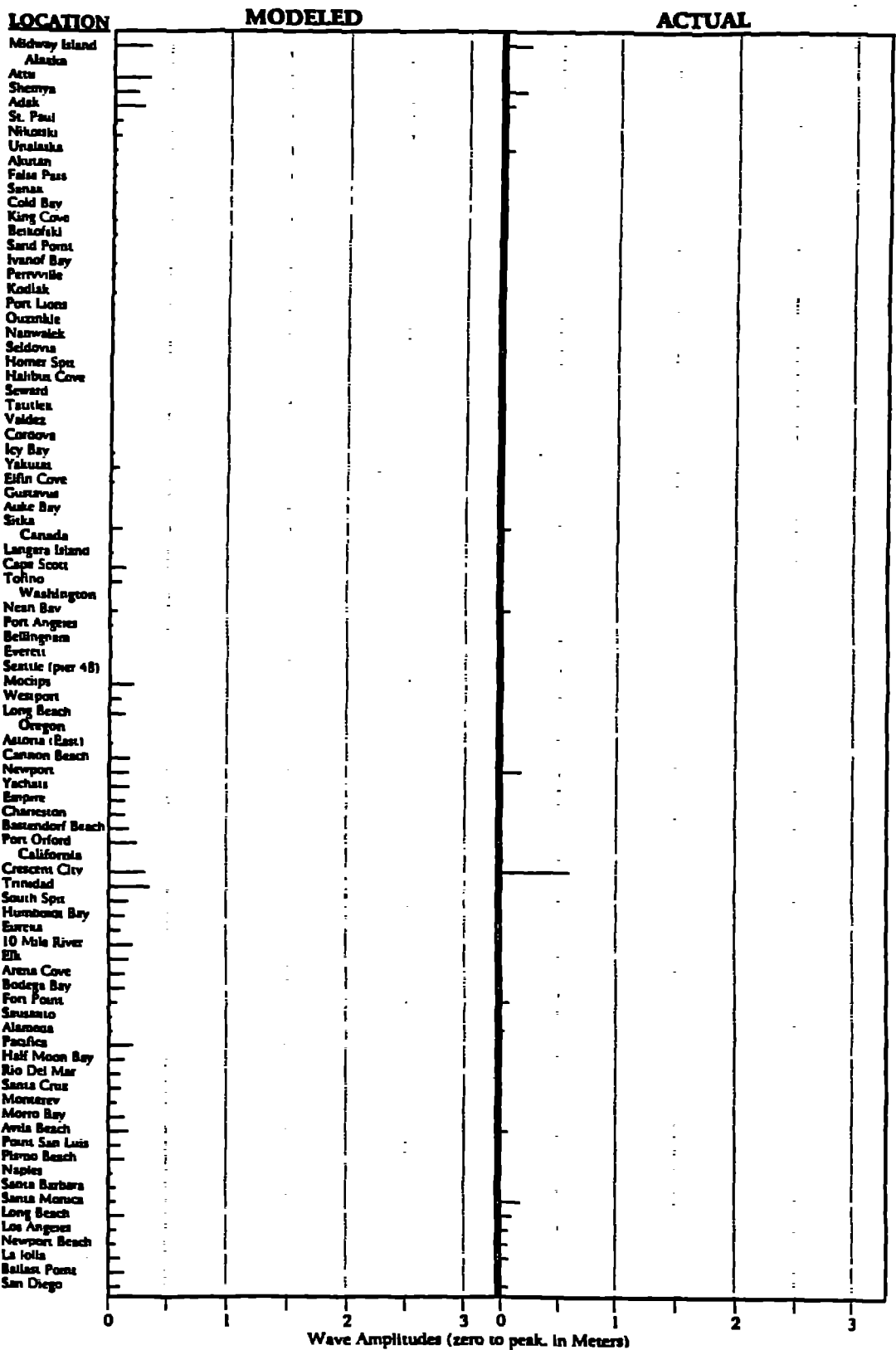
Figure 3.)   Comparison of recorded versus modeled amplitudes for the May 16, 1968 northern Honshu earthquake and tsunami. Amplitudes listed are zero-to-peak in meters. All tide gages which recorded a tsunami and had a model performed at that location are shown along with the other modeled amplitudes.

LOCATION   **MODELED**   **ACTUAL**

Midway Island
   Alaska
Attu
Shemya
Adak
St. Paul
Nikolski
Unalaska
Akutan
False Pass
Sanak
Cold Bay
King Cove
Belkofski
Sand Point
Ivanof Bay
Perryville
Kodiak
Port Lions
Ouzinkie
Nanwalek
Seldovia
Homer Spit
Halibut Cove
Seward
Tatitlek
Valdez
Cordova
Icy Bay
Yakutat
Elfin Cove
Gustavus
Auke Bay
Sitka
   Canada
Langara Island
Cape Scott
Tofino
   Washington
Neah Bay
Port Angeles
Bellingham
Everett
Seattle (prior 48)
Moclips
Westport
Long Beach
   Oregon
Astoria (East)
Cannon Beach
Newport
Yachats
Empire
Charleston
Bastendorf Beach
Port Orford
   California
Crescent City
Trinidad
South Spit
Humboldt Bay
Eureka
10 Mile River
Elk
Arena Cove
Bodega Bay
Fort Point
Sausalito
Alameda
Pacifica
Half Moon Bay
Rio Del Mar
Santa Cruz
Monterey
Morro Bay
Point San Luis
Pismo Beach
Surf
Naples
Santa Barbara
Malibu
Santa Monica
Los Angeles
Laguna Beach
La Jolla
Balast Point
San Diego

0   1   2   3   0   1   2   3

Wave Amplitudes (zero to peak, in Meters)

Figure 4.)   Comparison of recorded versus modeled amplitudes for the October 4, 1994 Kuril Island earthquake and tsunami. Amplitudes listed are zero-to-peak in meters. All tide gages which recorded a tsunami and had a model performed at that location are shown along with the other modeled amplitudes.
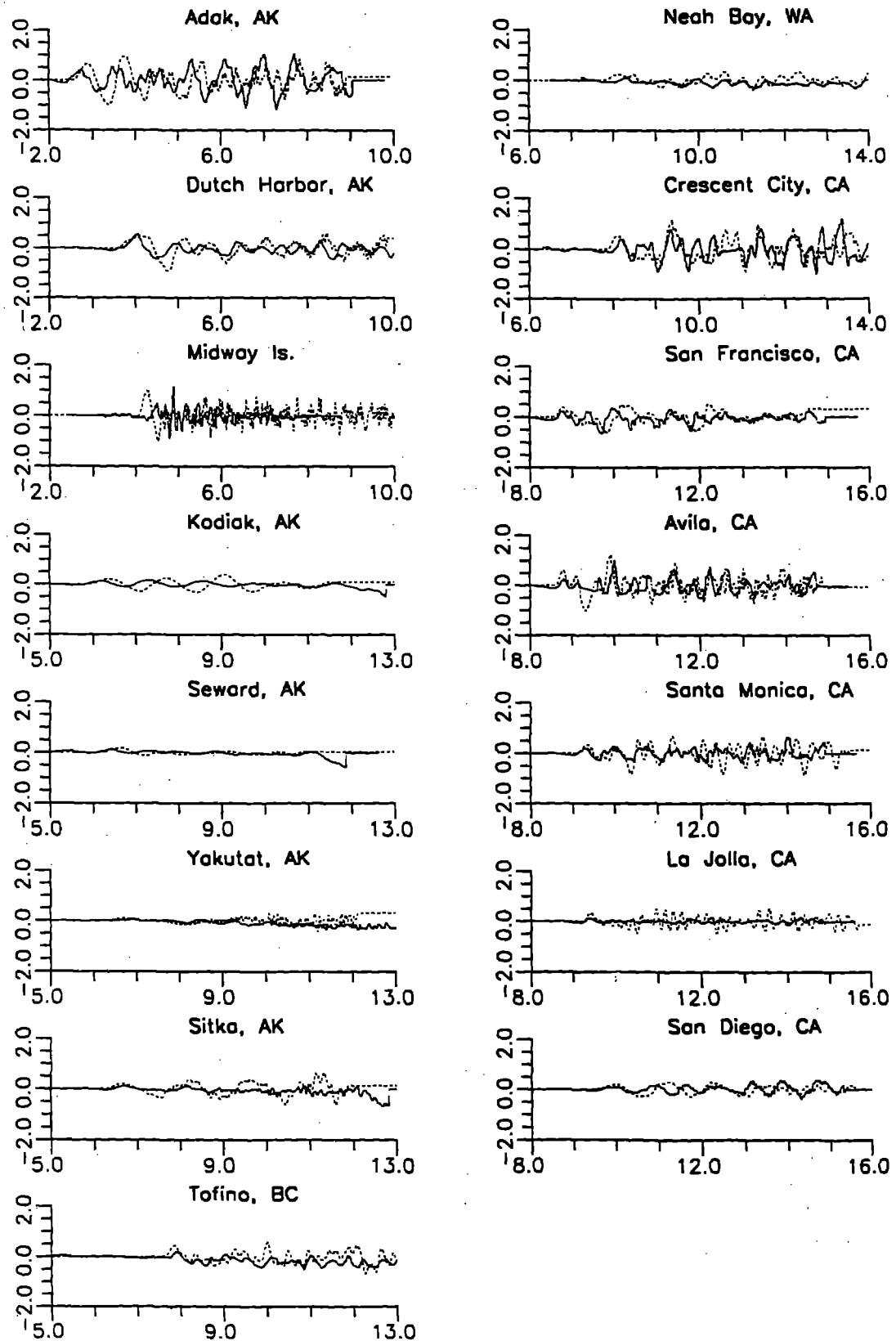
Figure 5.) Modeled tsunami with the recorded 1952 Kamchatka tsunami at tide gages in the ATWC AOR and Midway Island. Solid lines are the recorded tsunamis. Dashed lines are the modeled tsunamis. The recorded tsunamis were digitized from a U.S. Dept. of Commerce report (1953) and then high-pass filtered to remove the tide. The horizontal scale is time in hours relative to earthquake origin time. Vertical scale is sea level in meters. The unusual troughs on the Avila, CA recorded tsunami occur because the tide gage had reached its lower limit.

162
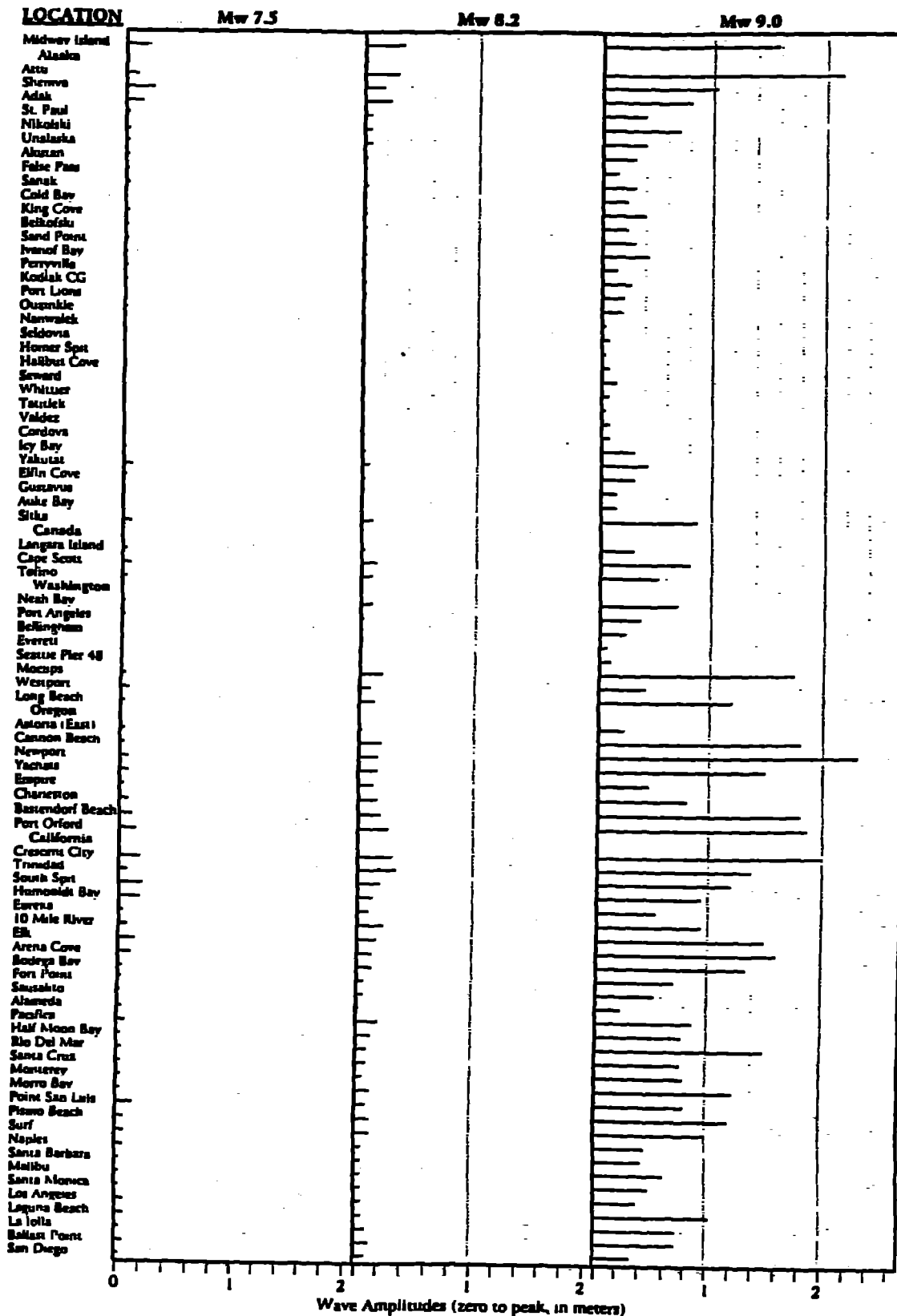
Figure 6.)   Modeled tsunami amplitudes for hypothetical earthquakes of Mw 7.5, 8.2, and 9.0 along the northern Honshu subduction zone.
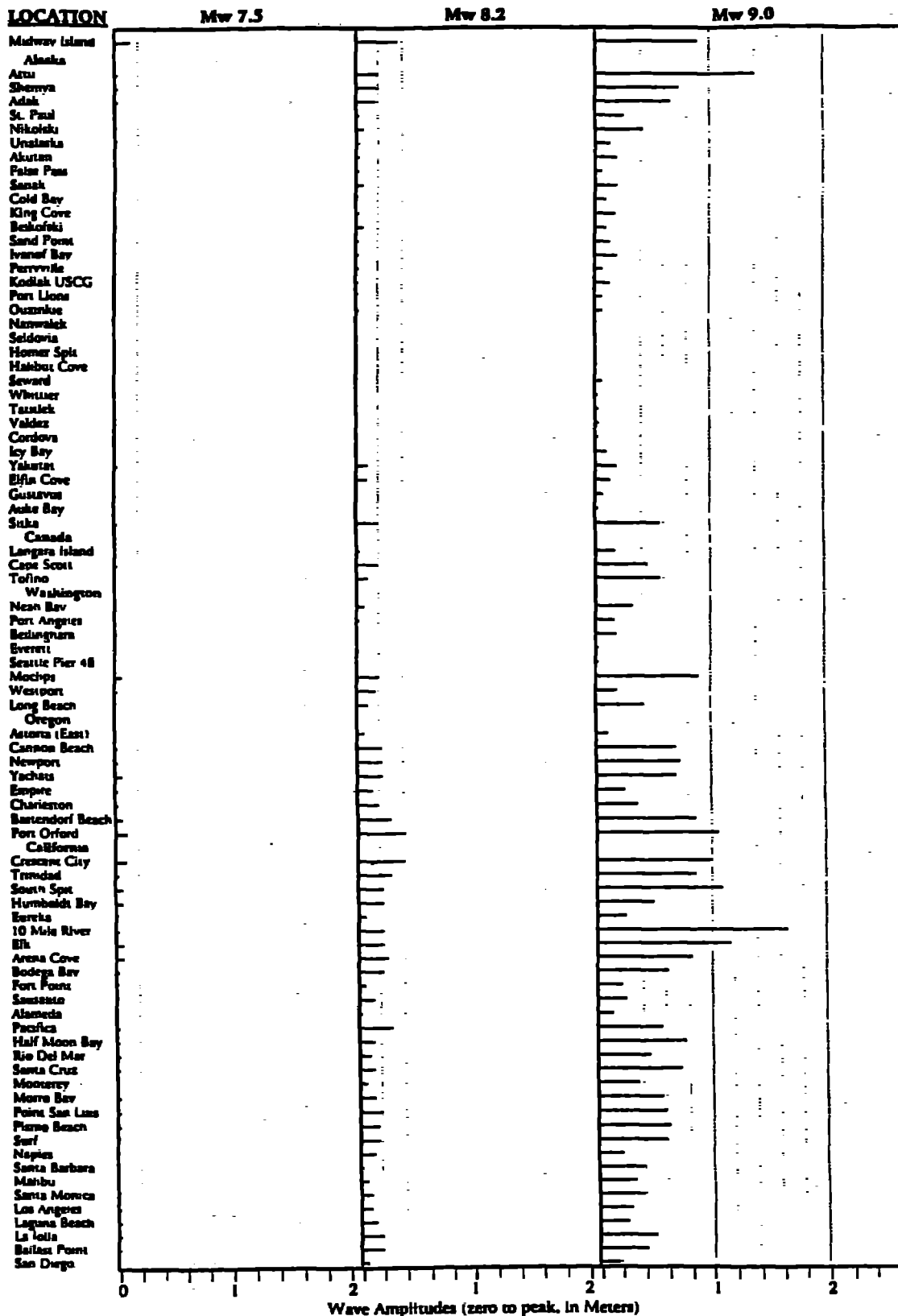
Figure 7.)   Modeled tsunami amplitudes for hypothetical earthquakes of Mw 7.5, 8.2, and 9.0 along the southern Kuril Islands subduction zone.

LOCATION Mw 7.5   Mw 8.2   Mw 9.0

Wave Amplitudes (zero to peak, in Meters)
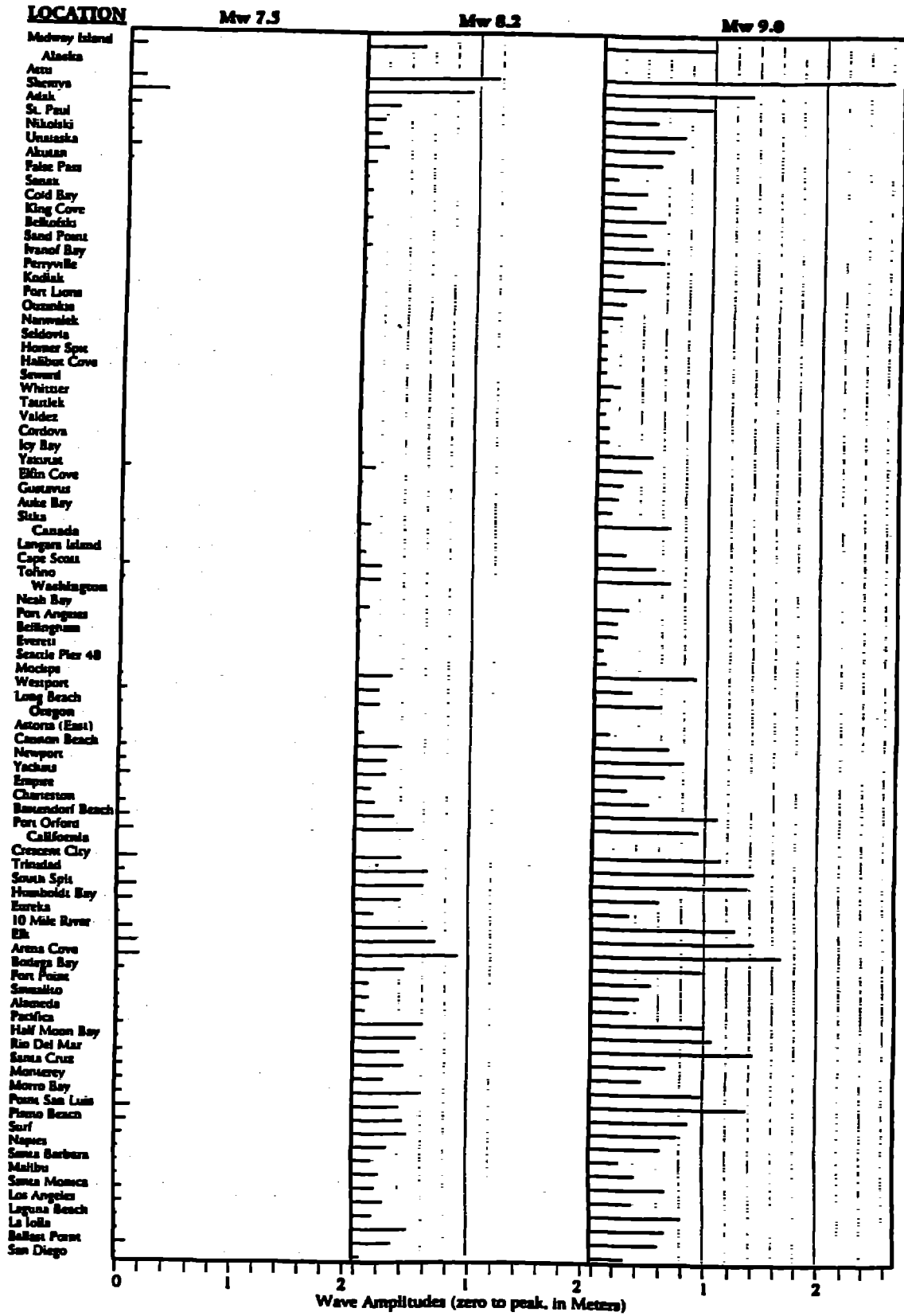
Figure 8.) Modeled tsunami amplitudes for hypothetical earthquakes of Mw 7.5, 8.2, and 9.0 along the northern Kuril Islands/southern Kamchatka subduction zone.

165
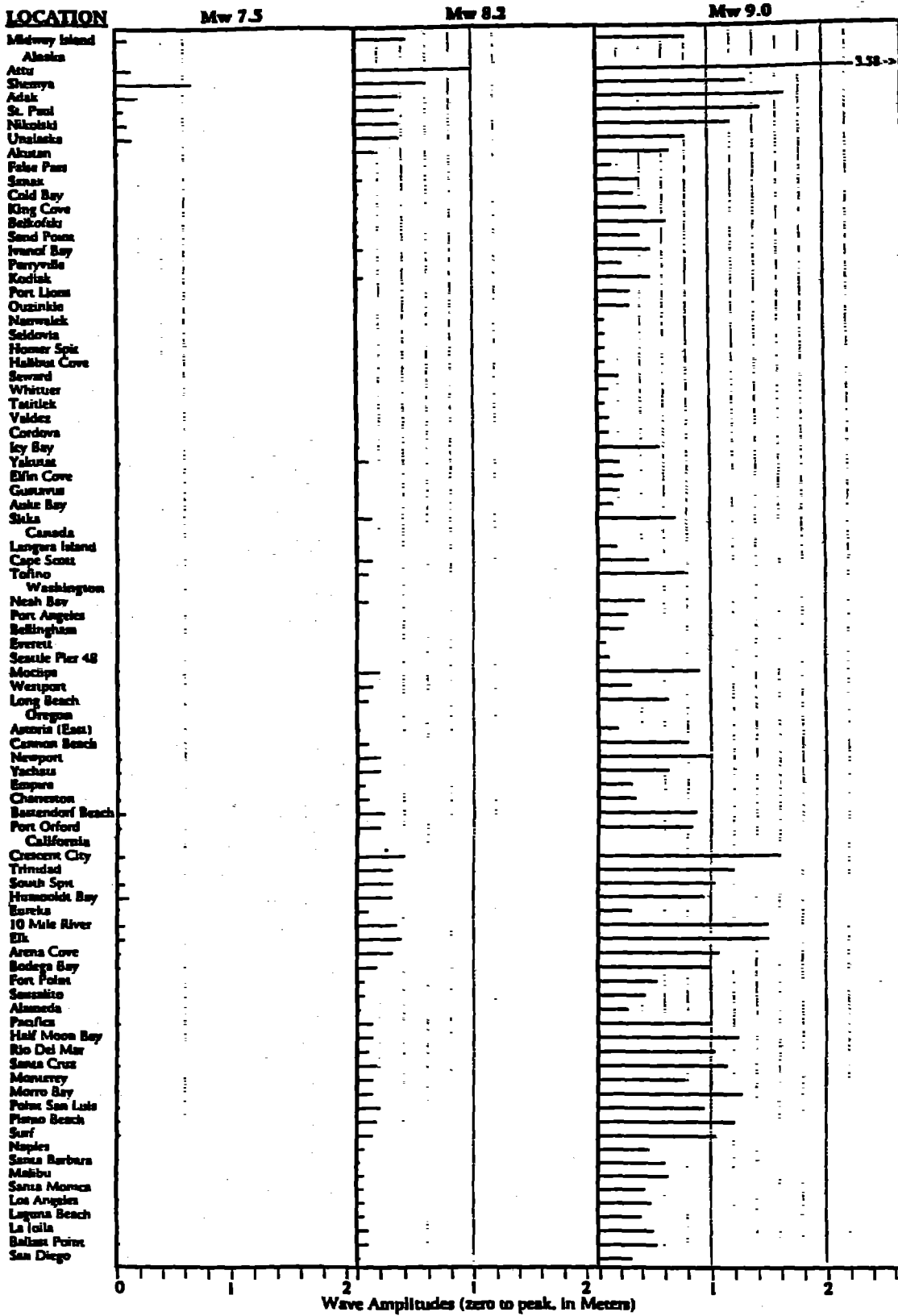
Figure 9.) Modeled tsunami amplitudes for hypothetical earthquakes of Mw 7.5, 8.2, and 9.0 along the Kamchatka subduction zone.
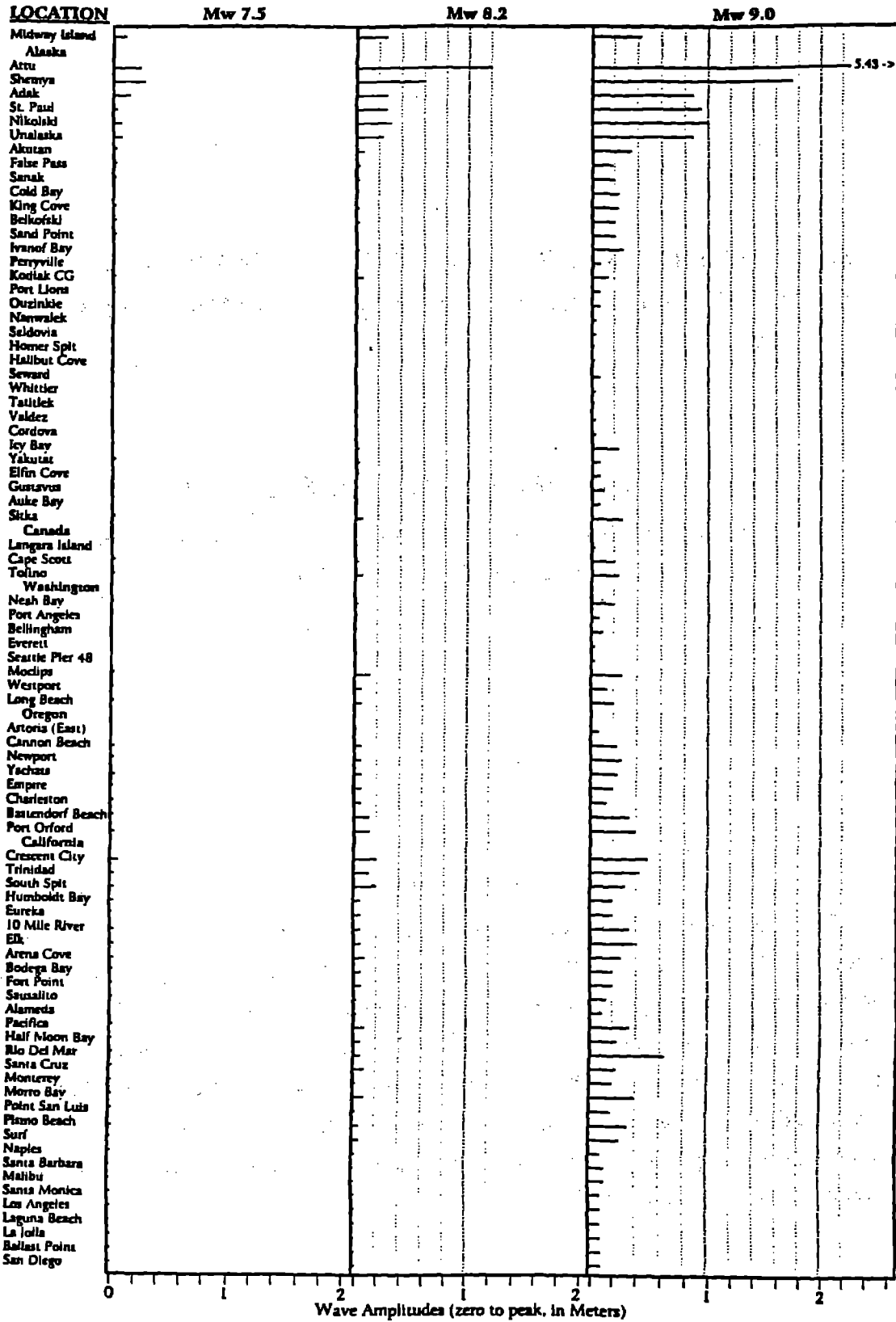
Figure 10.)   Modeled tsunami amplitudes for hypothetical earthquakes of Mw 7.5, 8.2, and 9.0 along the Commander Islands trench.

DAMAGES TO COASTAL STRUCTURES IN AWAJI AND TOBAN COASTS DUE TO THE 1995 HYOGOKEN NANBU EARTHQUAKE

Shigenobu TANAKA and Shinji SATO

Coastal Engineering Division, Public Works Research Institute

1 Asahi, Tsukuba, 305 JAPAN

ABSTRACT

This paper reports damages to coastal structures caused by the 1995 Hyogoken Nanbu Earthquake. Although no significant tsunami was generated, the strong seismic motion attacked coastal structures on Awaji Island, Toban coast and Kobe port, resulting in the collapse of coastal dikes and the failure of water gates in a wide area. Damages in Awaji and Toban coasts are described in detail. The authors point out that tsunami protection facilities such as coastal dikes and gates can be damaged by strong seismic motion so as to make them ineffective for tsunami flood countermeasure. Especially, damages to gates should not be disregarded because they will fail to be operated even in case of small damage.

I. INTRODUCTION

The Hyogoken Nanbu Earthquake occurred at 5:46 a.m. on January 17, 1995, Japan Standard Time. The magnitude of the earthquake was 7.2 on the JMA scale. Since the epicenter was very close to the highly-populated city of Kobe, more than 6,000 lives were lost by the earthquake. Catastrophic damages were caused on houses, high-storied buildings, port facilities, railways and highway bridges.

The epicenter of the earthquake was in the middle of the Akashi Straits (see Fig. 1). The earthquake was caused by the sliding motion of several active faults extending from the north of Awaji Island to the northern part of Kobe. Damages were especially large in a narrow band along the fault line, in which the seismic intensity reached 7 in JMA scale. Since only a fraction of the fault line was under the sea and the sea depth along the fault line was shallower than 100 m, no significant tsunami was observed. However, since the ground motion was tremendously large and resulted in large displacements in a wide area of coastlines, it caused significant damages on various coastal structures. This report describes damages of coastal dikes occurred on Awaji and Toban coasts and those of water gates in port of Kobe.
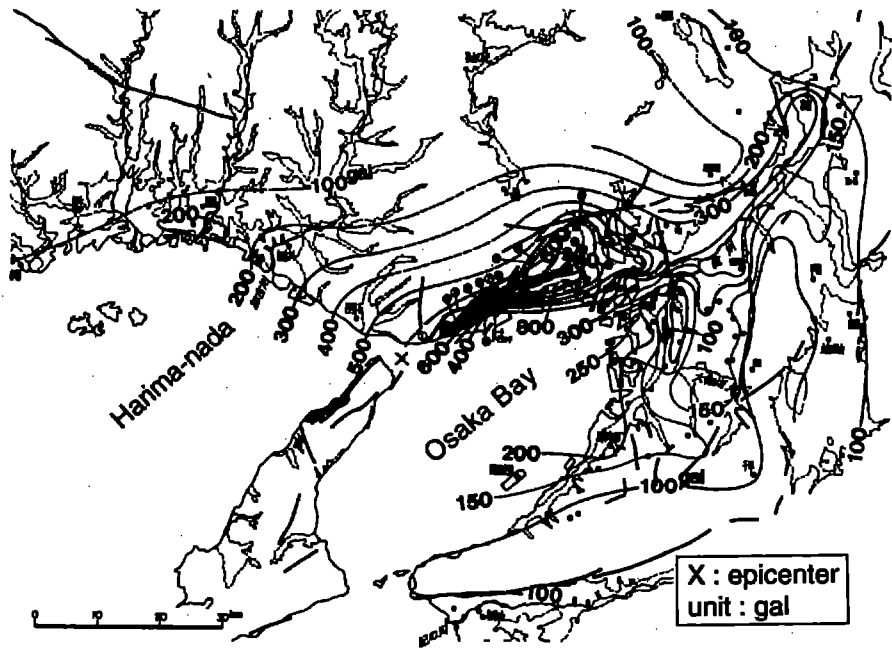
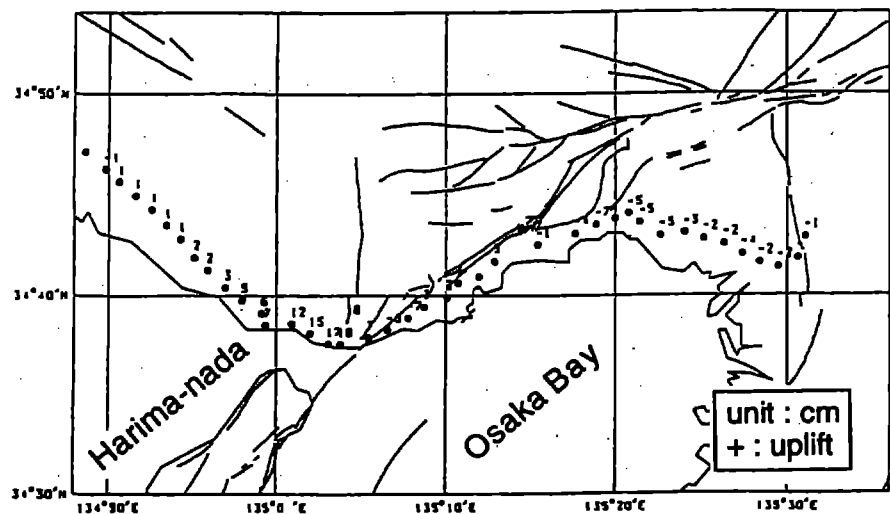Fig. 1 Distribution of Maximum Horizontal Accelerations

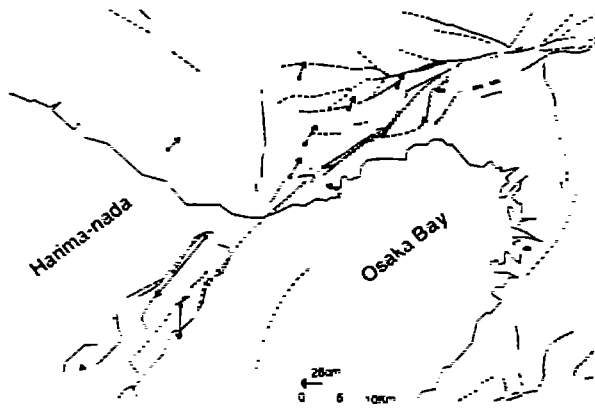Fig. 2 Distribution of Vertical Displacements of Ground

Fig. 3 Distribution of Horizontal
Displacements of Ground

II. OUTLINE OF THE EARTHQUAKE MOTION

Figure 1 illustrates the distribution of maximum horizontal accelerations compiled by the National Research Institute for Earth Science and Disaster Prevention, Science and Technology Agency. The area of large acceleration is located in an area from the southwest Kobe to the northeast. The maximum horizontal acceleration exceeded 800 gal (cm/s^2) in the north-south component, which was recorded at the Kobe Maritime Meteorological Observatory. On Toban coast, the maximum acceleration was 300 gal at the west end and 600 gal at the east end. Vertical acceleration was also large in this earthquake. The maximum vertical acceleration of 556 gal was recorded on Port Island, an artificial island located on the south of the central Kobe.

Figure 2 shows the distribution of vertical displacements of ground surveyed by Geographical Survey Institute after the earthquake. Relative uplift is noticed on the west side of the fault and settlement is noticed on the east side. The vertical gap at the fault line is about 30 cm, which is located at Suma coast in this figure. Figure 3 shows the distribution of horizontal displacements. On the north of the fault line, the ground was moved relatively to the northeast with displacement of 30 cm. On Awaji Island, the land on the southern side of the fault was moved to the southwest with displacements larger than 100 cm.

III. DAMAGES OF COASTAL PROTECTION FACILITIES

The Hyogoken Nanbu Earthquake was reported to have damaged coastal dikes and sea walls at 104 sections. The damage was concentrated in the cities of Kobe, Ashiya, Nishinomiya and Amagasaki, which accounted for 90 sections or 87% of the total.

Coastal dikes and sea walls may be classified from their dynamic properties into earth dikes (ordinary embankments covered by concrete), gravity-type dikes (concrete-type dikes which resist external forces with their own weight), and dikes with sheet or steel pipe piles (which resist external forces with stiffness). Damage was observed at 15 points on earth dikes, 52 points on gravity-type dikes and 37 points on sheet or pile dikes. Broken gravity-type and sheet or pile dikes were all located in Kobe, Ashiya, Nishinomiya or Amagasaki.

Seven coastal protection facilities other than coastal dikes or sea walls were damaged. They are listed in Table 1.

Coastal protection facilities are under the jurisdiction of four ministries or government agencies, i.e. the Ministry of Construction, the Ministry of Transport, and the Agricultural Structure Improvement Bureau and the Fisheries Agency of the Ministry of Agriculture, Forestry and Fisheries. Relatively few coastal areas in the southern part of Hyogo Prefecture are managed by the Ministry

Table 1 Damage to Coastal Structures other than Coastal Dikes or Revetments

administrator	harbor	facility	damage
Hyogo Prefecture	Amagasaki Nishinomiya	No.1 lock	destruction of main body of the lock
	Ashiya Harbor	revetment, sluice gate, ship lock	5 sluice gates and other facilities
Kobe City	Kobe Harbor	Owada water gate	exfoliation and cracks at the gate pillars
		Tsukishima water gate	exfoliation and cracks at the gate pillars
		Shinzaike water gate	exfoliation and cracks at the gate pillars
		Nadahama water gate	exfoliation and cracks at the gate pillars
		Uozaki No.2 pumping station	disconnection of joints at the drainage sluice gate and inflow of soil

of Construction. Of the 12 coastal protection facilities under the management of the Ministry of Construction which were damaged by the earthquake, 4 were along the Toban Coast and 8 on Awaji Island, such as those in the Matsuho District. All of these structures were earth dikes. The damage was relatively slight, such as settlement of dike crowns, disconnection of joints, or cracking, as shown in Table 2. Since there was only slight damage, these facilities were able to maintain

Table 2 Damage to Coastal Dikes and Revetments under the Jurisdiction of the Ministry of Construction

coast	facility	damage
Kariguchidai, Tarumi, Toban Coast	dike (buttressed wall)	-maximum settlement of 19 cm -cavities of 30 cm deep
Daikan-cho, Akashi Higashi, Toban Coast	dike (buttressed wall)	-maximum settlement of 27 cm -cracks between parapets and filled material (4.1 m deep and 5 cm wide) -cavities of 50 cm deep
Funage-cho, Akashi Higashi, Toban Coast	dike (buttressed wall and pile foundation)	-maximum settlement of 55 cm -cracks between parapets and filled material (0.6 m deep and 10 cm wide) -cavities of 20 cm deep
Eigashima, Okubocho, Akashi Nishi, Toban Coast	revetment	-maximum settlement of 4 cm
Matsuho, Awaji Coast	revetment	-maximum settlement of the revetment: 40 cm -maximum slide toward the sea: 15 cm -opening of joints: 20-30 cm -destruction of aprons and drain ditches
Kusumoto Higashi No.1, Higashiura Coast	revetment (concrete blocks)	-maximum settlement of the revetment: 50 cm -maximum slide toward the sea: 70 cm -slide of the hinter ground -opening of joints
Kusumoto Higashi No 2, Higashiura Coast	revetment (concrete blocks)	-maximum settlement of the landward side: 20 cm -maximum slide toward the sea: 30 cm
Kuruma, Higashiura Coast	dike	-maximum settlement of the dike: 5 cm -maximum slide toward the sea: 4 cm -opening of joints
Tsui, Seitan Coast	revetment	-damage to the foundation, revetment and road for maintenance
Tsunokawa, Goshiki Coast	revetment	-damage to road for maintenance
Nojima No.1, Hokutan Coast	revetment	-maximum settlement of the revetment: 5 cm -maximum slide toward the sea: 10 cm -cracks
Nojima No.2, Hokutan Coast	revetment	-cracks at and destruction of the parapet wall

most of their functions.

On the other hand, most of the coastal facilities under the jurisdiction of the Ministry of Transport were heavily damaged and some of them lost their function. All of them were of gravity-type or sheet pile type. Photo 1 shows damage to a gravity-type dike at Ashiya Port. The damage was as follows: The parapets were settled unequally. The joint opened up to 68 cm. The crown was heavily broken.

Photo 1 Damage to Coastal Dike in Ashiya Port

IV. DAMAGES TO COASTAL DIKES AND REVETMENTS

IV-1. Typical Examples of Damage to Coastal Dikes and Revetments

(1) Awaji coast

Since the horizontal ground displacement was extremely large on Awaji Island, most of the failures of coastal dikes occurred where land slip or land slide were also observed nearby. Wide gaps of 30 to 50 cm were found at the joint section of dikes.

At the Matsuho District, located at the north end of Awaji Island, the maximum settlement of parapets was 40 cm, the greatest settlement of dike crown aprons was 60 cm, and the largest slide toward the sea was 15 cm. The joint of the dike disconnected for about 20 cm at the dike crown and for 30 cm at the base due to slide along the dike as shown Photo 2(Sumoto Construction Office,1995).
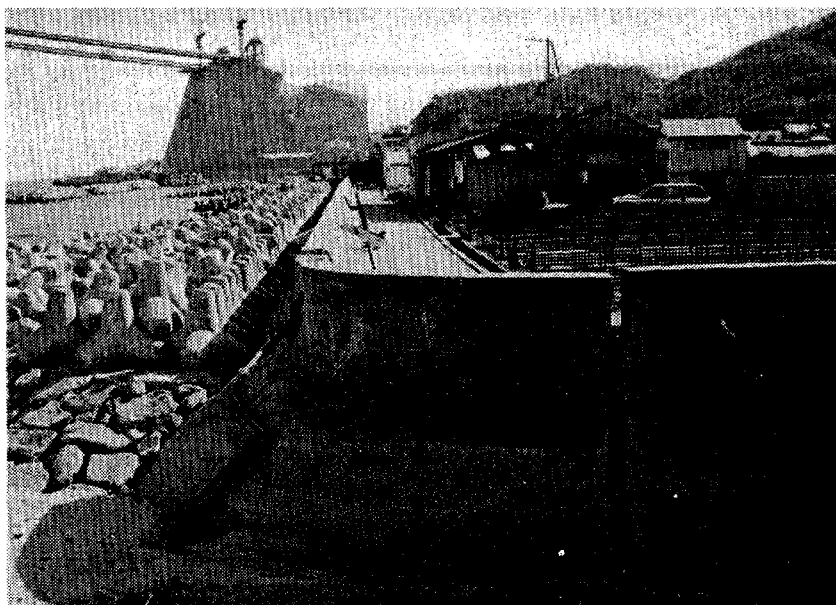

Photo 2 Damage to Coastal Revetment along the Awaji Coast (Matsuho)

The joints of seaward slope covering opened for approximately 20 cm at its top.

(2) Toban coast

Figure 4 shows a location map of the sites along Toban

coast on which significant damages to coastal structures are observed. Compared to the coasts in northern Awaji Island, seismic motion on Toban coast was relatively weak (see Fig. 1). The damage pattern of coastal dikes was mostly the settlement of parapet and lateral spreading of the body to the land side of the dike (see Fig. 5). The maximum settlement reached 55 cm at the right bank of Akashi River. On most of the sites where significant settlements were observed, the settlement of filled materials was also observed, leading to the presence of a cavity beneath the parapet. The presence of the cavity and the lateral spreading to the land side suggests that the filled materials settled by the strong seismic motion. It is noticed from Fig. 4 that the failure sites are mostly located near the river

Fig. 4 Location Map of Toban Coast

Fig. 5 Typical Damages to Coastal Dike

mouthes, where the structures were based on rather soft foundation, the thickness of mud layer is more than 15 m. Though the degree of damage in Toban coast was low, the failure of dikes along Toban coast strongly depends on the soil characteristics of the foundation.

Figure 6 illustrates a cross section of the damaged coastal dike in Daikan-cho, located at the left of the river mouth of the Akashi River, on the Toban Coast. Only the filling deformed and settled due to earthquake motion. The coastal dike in Funage-cho, located on the right bank of the mouth of the Akashi River, was similarly stricken by the earthquake. Although the damage to Funage-cho dike was worse than of Daikan-cho, the settlement of both dike crowns was slight, i.e., 5-10% of the bank height of 5 m.

Figure 7 shows a geological cross section of these area. The rigid soil under the dike at Daikan-cho may have avoided severe damage(Fig. 7 left). As shown in the right side of Fig. 7, the lower part of Funage-cho dike has a pile foundation because the soil is relatively weak. As mentioned above, the damage to Funage-cho dike was just worse than that of
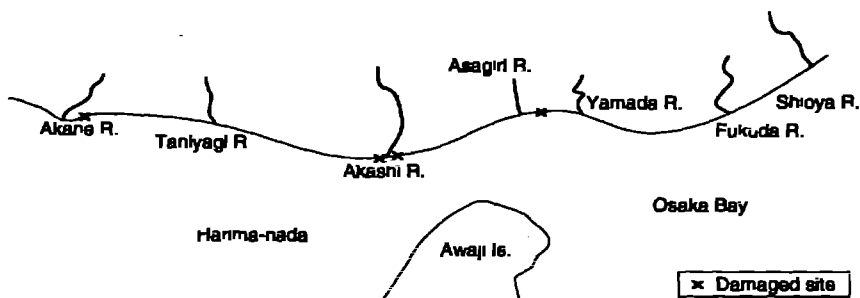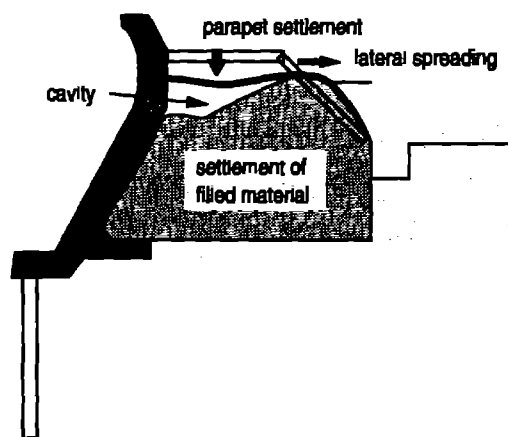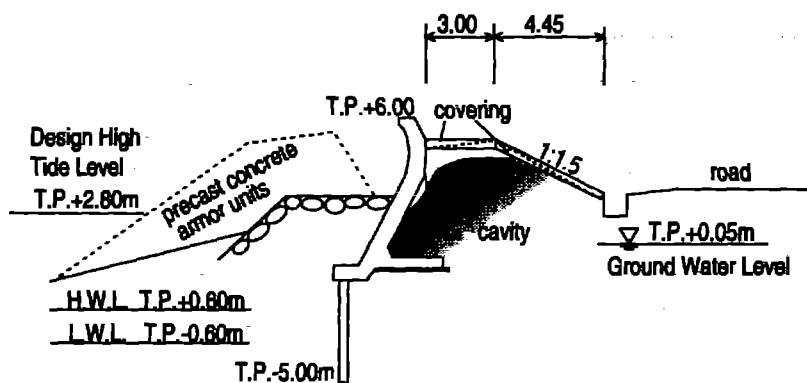

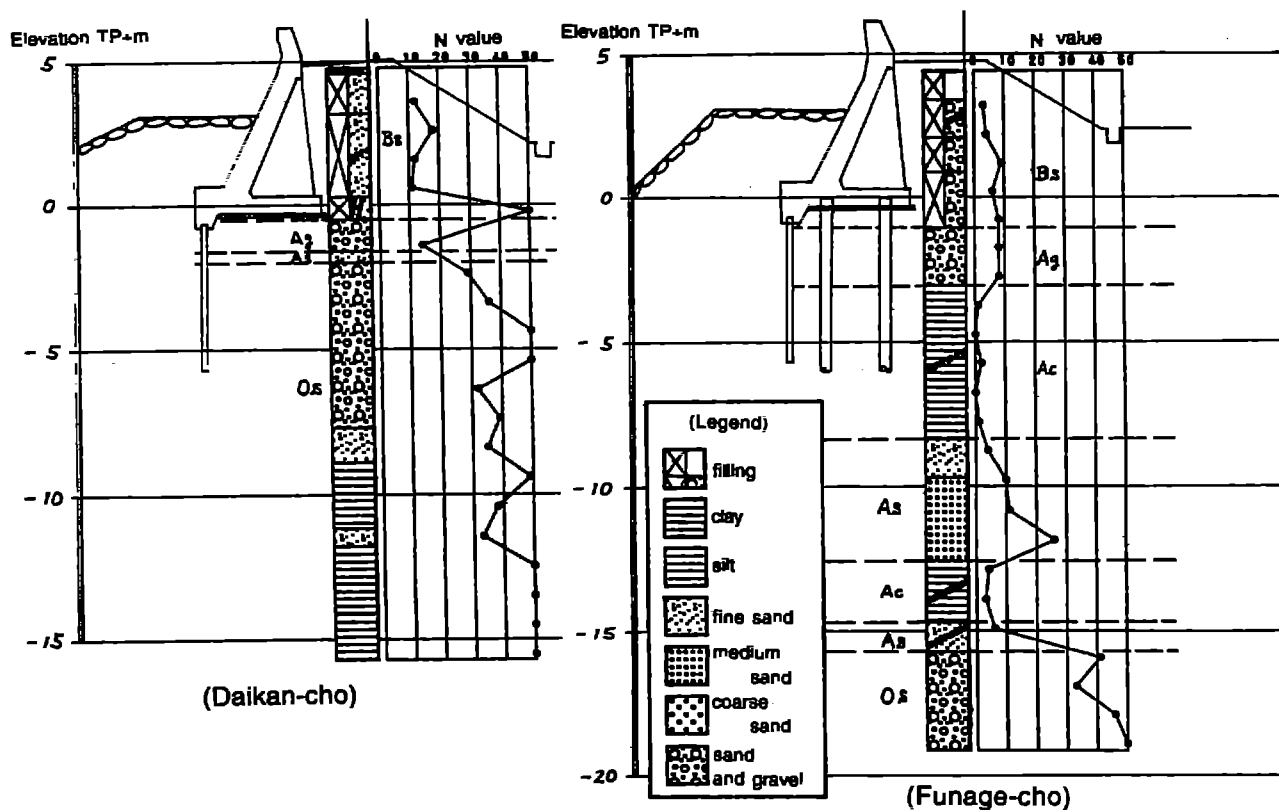Fig. 6 Damage to a Coastal Dike along the Toban Coast
(Daikan-cho, Akashi)

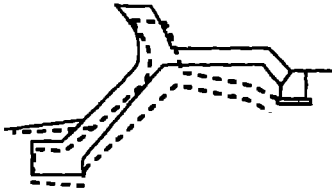Fig. 7 Geological Cross Section under a Coastal Dike along the Toban Coast
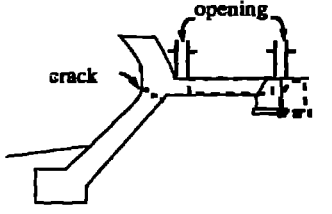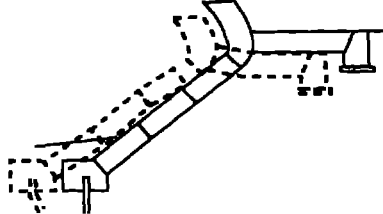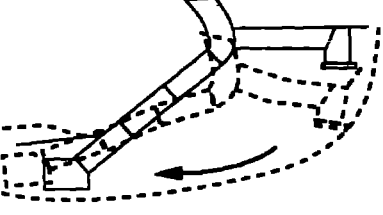
Daikan-cho, though the condition of the ground was rather weak. Damage to other sections of Toban Coast was all related to the dike structure and was not attributable to their foundations. As these cases show, as to Toban coast, foundations suitable for each type of soil may rather reduce the damage attributable to the ground characteristics at the foundation of a dike.

IV-2. Characteristics and causes of damage to earth dikes and revetments

IV-2.1. Classification of damage due to earthquake

The damage to earth dikes by the earthquakes which occurred between Kushiro-oki Earthquake in 1993 and the Hyogoken Nanbu Earthquake may be classified into the 4 patterns shown in Table 3. Damage pattern I includes settlement of all or part of a dike or revetment. The Hyogoken Nanbu Earthquake caused a maximum settlement of 55 cm in a dike along the Toban Coast. Hollow spaces or cavities were created under many other dikes covered with concrete. Damage pattern II includes disconnection at joints between concrete structures such as parapets, and cracks at foundations and around joints. This pattern represents typical earthquake damage, and was frequently observed in this earthquake. Damage pattern III includes slide of seaward slope covering concrete, which are caused by cracks or disconnections of joints. The slide may be accompanied by settlement of filling and lateral spreading. This earthquake also caused such damage (coastal dikes on Awaji Island). Damage pattern IV includes sliding collapse of dike and adjacent hinter ground, which may be accompanied by the settlement of dike, the destruction, cracking, or disconnecting of concrete structures. This damage is rare, and no such case was observed in this earthquake. Figure 8 shows

Table 3 Classification of Earthquake Damage to Dikes and Revetments

pattern	major damage	schematic diagram of damage	characteristics of damage
I	settlement of dike or revetment		· Either all or part of dike or revetment settled. · Crustal movement also caused such settlement.
II	cracks, breaking, settlement		· A concrete structure broke, cracked or opened at a joint. · Parapets broke, cracked or inclined. · Aprons broke, cracked, or opened at a joint. · This damage frequently accompanied settlement of the filled material at the back of parapets.
III	slide of slope covering (settlement, lateral spreading)		· Concrete covering over slopes slid by the cracking or opening at a joint. · Slide of slope covering sometimes accompanied settlement or bulging of the slopes. · This damage frequently accompanied breaking, cracking and/or disconnection of concrete structures.
IV	sliding collapse		· The dike and adjacent hinter ground collapsed by sliding. · This damage frequently accompanied settlement. · This damage frequently accompanied breaking, cracks and/or disconnection of concrete structures.

the frequency of each damage type from 1964 (Niigata Earthquake) to 1995 (Hyogoken Nanbu Earthquake). Damage patterns I and II were common for dikes and pattern II was most common for revetments.

These damage patterns are only a simple morphological classification. Many damage cases cannot be categorized as one specific pattern but show characteristics of two or more patterns. Causes of damage may be the earthquake inertial force and/or decrease in the bearing capacity of the basement ground due to liquefaction. These causes are not directly connected with damage patterns but act complexly.

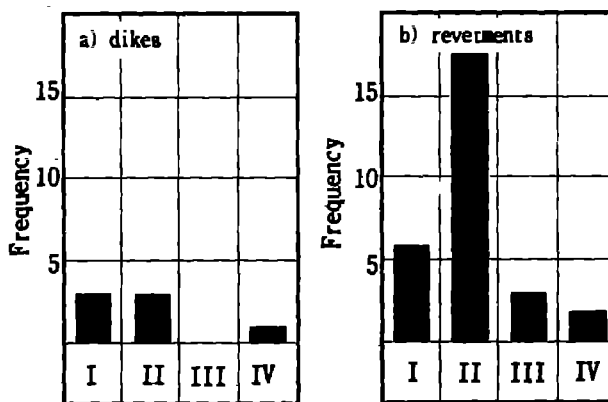The main factor for damage pattern I was

Fig. 8 Patterns of Earthquake Damage to Coastal Dikes and Revetments

probably a decrease in the bearing capacity of the liquefied ground. Compaction of filled materials by the earthquake motion could also account for slight settlement. Most of damage pattern II was probably caused by seismic motion. There were many cases of uneven settlement. Some of them might suggest a decrease in the bearing capacities of the basement ground due to liquefaction. The factor for damage pattern III was also probably seismic motion. Some cases of settlements may have been caused by slide of basement of covering concrete. There were cases accompanied by the liquefaction of the basement ground. The likely main factor for the damage pattern IV was also seismic motion. However, many cases of sliding collapse could have been caused by the liquefaction of the adjacent hinter ground.

Damage by tsunamis, which occurs immediately after earthquake, is mostly attributable to overflow. The Hyogoken Nanbu Earthquake, however, generated only small-scale tsunamis and caused no such damage.

IV-2.2. Characteristics and causes of damage
1) Characteristics of damage

The number of coastal earth dikes and revetments damaged by the Hyogoken Nanbu Earthquake was 11 facilities on Awaji Island (8 under the jurisdiction of the Ministry of Construction, 1 under the Agricultural Structure Improvement Bureau, and 2 under the Fisheries Agency) and 4 facilities along the Toban Coast. The outlines of the damage have already been described in previous sections. Although the dikes and revetments were located near the epicenter, they were just slightly damaged and could function relatively well after the earthquake, except for one whose joint disconnected significantly.

The damage distribution did not altogether correspond with the distances from the epicenter. The degrees of the earthquake motion, i.e. acceleration, on Awaji Island and the Toban Coast, where relatively many earth dikes and revetments have been built, are not clearly known, but can be estimated from Fig. 1 to be 200 gal or more in the horizontal direction and to correspond with the distances from the epicenter. The fact that damaged facilities were scattered over a large area and that the damage was slight suggests the involvement of ground conditions.

With respect to the damaged section of earth dikes and revetments, sand boils, which are the traces of ground liquefaction, were observed only in the Kusumoto Higashi District along the Higashiura Coast of Awaji Island.

2) Causes of damage

Earth dikes may not be designed to resist earthquakes since they are easy to repair even after being damaged by earthquakes. The slight damage to such dikes by the Hyogoken Nanbu Earthquake may be attributable to rather good ground conditions. According to a survey conducted after the earthquake, the ground at the basement of earth dikes and revetments on Awaji Island is composed of hard sandy or pebbly soil, and loose sandy layer which is susceptible to liquefaction is rare. Most of the ground along the 20 km Toban Coast is either solid rock, hard diluvial pebbly and

sandy soils, or relatively hard clayey soils. The basement ground along the Toban Coast is solid rock in the section between Suma-ku of Kobe City and the Fukuda River (Rokko granite and Kobe layers), and is composed of hard diluvial clayey, sandy and pebbly soils (Osaka layers) west of the Fukuda River. Alluvial layers, which are distributed along small and medium size rivers running into Akashi Straits or the Sea of Harima(Harima-nada), are the poor ground. But the layers exceeding 10 m in thickness exist only along the Shioyatani, Fukuda, Yamada, Asagiri and Akashi Rivers.

Damage to coastal facilities along the Toban Coast by the earthquake was scattered over the entire 20 km coast line and was independent of the distance from the epicenter. The relationship between the damaged earth dike or revetment and its basement ground shows that the damage in the sections of solid rock or diluvial layers was slight while the damage in alluvial soils was serious. The alluvial layers along the Shioyatani, Yamada and Akashi Rivers, where damage was serious, are all 15 m - 25 m thick and are composed of loose sand and soft clay. The stability of four damaged facilities along these rivers was investigated by estimating the intensity of the seismic motion from Fig. 1. In case of considering inertia forces, it resulted in that three of these facilities were unstable. The facility along the Akashi River showed an especially low value, much smaller than 1. Furthermore, a conventional estimation on liquefaction indicates that it may have occurred at three points, especially at a point along the Akashi River, where the dike subsided for 55 cm (parapets, however, did not sink much). In other words, the damage was less serious than expected because the loose sandy layer, which is susceptible to liquefaction, was only 5 m thick at this point.

Damage to earth dikes and revetments caused by the Hyogoken Nanbu Earthquake was slight overall although they were located near the epicenter. This may be attributable to the relatively good condition of the basement ground, especially to a limited distribution of loose sandy soil, which is vulnerable to liquefaction. Structures, such as large-scale wave dissipating works and hard covering works, which resist waves and other external forces, may have potentially enhanced the resistance against earthquakes.

V. DAMAGES OF WATER GATES AND OTHER FACIL- ITIES

Water gate is a composite structure usually made of steel and concrete. On southern coasts of Hyogo prefecture, many water gates were installed to protect land from storm surges. As shown in Table 1, some of them were damaged. Photo 3 shows the damage to a pillar of Owada water gate. The concrete of the gate pillar was

Photo 3 Damage to Owada Water Gate

exfoliated. Even if the damages of the water gates look trivial, they sometimes fails to be operated since the mechanical portion are fragile against strong seismic motion. Electricity shutdown may sometimes be a crucial problem in maintaining the operation.

Photo 4 shows the damage to a gate in Kobe Port. The gate inclined 5 degree landward. Some cracks was made at the basement of the gate. It made the gate hard to be operated.

Fortunately in the 1995 Hyogoken Nanbu Earthquake, no tsunamis were generated and no storm surges attacked water gates damaged by the quake. However, it should be reminded that the functionality of

Photo 4 Damage to Gate in Kobe Port

water gate and other facilities, which should be operated in case of tsunami or storm surge, may sometimes be ceased after it experienced strong seismic motion.

VI. CONCLUDING REMARKS

The damages of coastal structures caused by the 1995 Hyogoken Nanbu Earthquake were apparently small compared with the tremendous damages occurred in the urbanized area of Kobe city. However, many coastal structures were collapsed by the historically strong seismic motions. Coastal dikes on northern Awaji Island were found to be collapsed owing to large ground displacements, resulting in a wide gap of 30 to 50 cm at the joint section. On Toban coasts, where seismic motion was relatively weak, the settlement of coastal dikes mostly occurred where they were based on thick mud layers near river mouths. Many water gates also suffered significant damages.

As to countermeasure against tsunamis and storm surges, the last protective line like castle continuously consists of coastal dikes, revetments, gates and water gates. The damages described above suggest a concern about the functionality of coastal dikes and tsunami gates in case that they are attacked by both strong seismic motion and tsunamis. Especially, at this earthquake disaster, dikes and revetments kept their functions but some of gates lost them. It should be focused on the facilities that must be shut in case of tsunami or storm surge and are usually open. Furthermore, since Japan is very mountinous, many people live along coastal flat. There are also some such facilities even in the village along Sanriku Coast, which was devastated by Meiji Sanriku Earthquake Tsunami 100 years ago. Therefore, such kind of problem is not only for coast of urbanized cities but for all coasts in Japan.

178   Acknowledgments

We would like to express our thanks to Himeji Work Office, Harbor Section of the Hyogo Prefectural Government and Sumoto Construction Office for providing photographs of damaged facilities and related data.

References

Sumoto Construction Office, Records of damage on Awaji Island Caused by the Hyogoken Nanbu Earthquake, 1995.

SPECTRAL DECOMPOSITION IN THE WAVE PROPAGATOR

APPROACH TO FINITE-ELEMENT TSUNAMI MODELING

Stefano Tinti, Elisabetta Bortolucci and Alessio Piatanesi

Università di Bologna, Dipartimento di Fisica,
Settore di Geofisica, Viale Berti Pichat, 8
40127 Bologna, Italy.

ABSTRACT

Linear Finite-Element models of long waves in shallow waters can be put in such a form that their solution can be computed by applying a linear operator to the initial source field: this linear operator was called the "wave propagator" of the problem. The general formal properties of the wave propagator were proven and illustrated in two previous papers. Here the representation of the solution in terms of the finite-element grid eigenmodes and grid time constants is explicitly derived and discussed.

Introduction

Tsunami propagation in the open sea can be described by the shallow-water approximation, that for many purposes results to be adequate even for near-shore tsunami evolution. The hydrodynamic equations governing the wave motion for an ideal inviscid fluid can be written as follows:

$$\begin{cases} \partial_t \zeta = -\partial_x(hu) - \partial_y(hv) \\ \partial_t u = -g\partial_x\zeta \\ \partial_t v = -g\partial_y\zeta \end{cases} \tag{1}$$

where ζ, u and v are functions of the space coordinates x and y and of the time t, and respectively denote the sea water elevation above the mean sea level and the horizontal components of the water velocity. Furthermore g is the gravity acceleration and the sea bottom $h(x,y)$ is assumed to be independent from the time. The space discretization of the system (1) over a finite-element grid consisting of N nodes transforms it to a system of $3N$ equations where the unknown time functions are the water elevation $\zeta_j(t)$ and horizontal velocities $u_j(t)$ and $v_j(t)$ at each grid node j. If we designate by $\bar\xi(t)$ the $3N$-component vector defined as:

$$\bar\xi_j(t) = \begin{cases} \zeta_j(t) & 1 \le j \le N \\ u(t)_{j-N} & N+1 \le j \le 2N \\ v(t)_{j-2N} & 2N+1 \le j \le 3N \end{cases} \tag{2}$$

the governing equations, inclusive of the conditions over the grid boundaries, were proven to be amenable to the form (Tinti and Piatanesi, 1995):

$$\begin{cases} d_t\bar\xi(t) = C\bar\xi(t) \\ \bar\xi(0) = \bar\xi_0 \end{cases} \tag{3}$$

where d_t denotes the total derivative with respect to the time. Here the matrix C is a square 3N by 3N matrix with constant real coefficients, whereas $\bar\xi_0$ is the $3N$ vector representing the known condition at the initial time $t = 0$. The solution to the system (3) can be found with the method of the spectral decomposition, consisting in factorizing the operator C in the product:

$$C = E\Lambda E^{-1} \tag{4}$$

where Λ is the diagonal matrix composed of the $3N$ eigenvalues of C and E is the corresponding eigenvector matrix, that is a matrix whose column j is the j-th unit eigenvector, say $\bar e_j$, of C associated with the eigenvalue λ_j; or more formally:

$$E = (\bar e_1, \bar e_2, ..., \bar e_{3N}) \quad C\bar e_j = \lambda_j \bar e_j \quad |\bar e_j| = 1 \tag{5}$$

The matrix E^{-1} is the inverse of E and it is conveniently interpreted as being formed of row vectors; more precisely, if we define by $\bar{f_j}$ the vector composed by the coefficients of the j-th row of E^{-1}, we may accordingly write:

$$E^{-1} = \begin{pmatrix} \bar{f_1} \\ \bar{f_2} \\ \vdots \\ \bar{f}_{3N} \end{pmatrix} \qquad (6)$$

The system of first-order differential equations (3) admits the unique solution:

$$\bar{\xi}(t) = P(t)\, \bar{\xi_0} \qquad P(t) = E e^{\Lambda t} E^{-1} \qquad (7)$$

where $P(t)$ is the wave propagator, i.e. is a linear operator depending only on time t that reduces identically to the unit matrix I as $t = 0$ and that, likewise C, is expressed in a factorized form. Important formal properties of the wave propagator have been already shown and discussed in two previous papers (Tinti and Piatanesi, 1995; Tinti et al., 1996) to which the reader may refer. Here, it is worthwhile reflecting on the meaning of the spectral representation of the solution $\bar{\xi}(t)$ that, in agreement with the expression (7), results to be a linear combination of the eigenmodes of C, each one evolving according to an exponential law with a specific time constant.

Spectral Representation of the Solution

The decomposition of the basic real matrix C given in (4) implies taking into account a $3N$ complex vector space, say S, since C admits complex eigenvalues and eigenvectors. In other words all the matrices E, Λ and E^{-1} are complex, but in virtue of the fact that they derive from a real matrix, they have an important property, that will be illustrated hereafter and that will be used to propose a simple spectral representation of the solution $\bar{\xi}(t)$.

Before dealing this aspect, however, it is convenient to make some preliminary considerations. First of all we observe that the basis of the eigenvectors $\bar{e_j}$ of C is complete, and consequently that any vector of the complex space S can be written uniquely as a linear combination of these eigenvectors. In order to prove the above sentence we will proceed in two steps, by taking however for given on the basis of fundamental algebra theorems that: 1) a real matrix C of dimension $3N$ admits exactly $3N$ eigenvalues, if the eigenvalue multiplicity is allowed for; and 2) a basis of a $3N$ vector space is complete if and only if it consists of $3N$ linearly independent unit vectors. In the first place it is easy to demonstrate that different eigenvalues λ of C are associated with linearly independent eigenvectors $\bar{e}$. From the hypothesis that $C\bar{x}_1 = \lambda_1 \bar{x}_1$ $C\bar{x}_2 = \lambda_2 \bar{x}_2$ with $\lambda_1 \neq \lambda_2$, it follows the thesis that $\bar{x}_2$ is linearly independent from $\bar{x}_1$, that is $\bar{x}_2$ is not proportional to $\bar{x}_1$. In fact if we rejected the thesis, we would get the contraddiction that the hypothesis would be false. Therefore, in the special case that all eigenvalues

of C are different from each other, the completeness of the eigenvector basis is proven. For the second part of the demonstration we observe that if there is an eigenvalue λ with multiplicity k, there will exist a subspace of S with dimension k, say S_k, with the property that any vector $\bar{x}$ of S_k is an eigenvector of C: $C\bar{x} = \lambda\bar{x}$. Consequently it is possible to find k unit vectors of S_k that are independent from each other forming a basis in S_k and that, being linearly independent from all other eigenvectors with different eigenvalues, form a distinct sub-basis in S. As a special case of this last category we can consider the null subspace of C, that is the space formed by all the vectors $\bar{x}$ satifying the equality $C\bar{x} = 0$. They all can be considered eigenvectors of C corresponding to the real eigenvalue $\lambda = 0$. Combining the two steps above, we can conclude that the basis formed by the eigenvectors associated with the simple eigenvalues and in addition by the eigenvectors of the sub-bases associated with the multiple eigenvalues are linearly independent and as many as the eigenvalues, and therefore constitute a complete basis. An immediate consequence of the basis completeness is that the eigenvector matrix E, having linearly independent columns, is of rank $3N$ and hence admits the inverse E^{-1}, as we had already assumed in the foregoing, though with no specific demonstration. A further consequence is that all the vectors $\bar{f}$ are linearly independent: bearing in mind the definition (6), this descends from the fact that the matrix E^{-1}, admitting the inverse, is thus of rank $3N$ and has linearly independent rows. Notice that the vectors $\bar{f}$ do not constitute a vector basis since in general they are not unit vectors.

The property that any vector of S admits a unique representation over a basis of vectors that is complete is a fundamental property of a vector linear space and deserves no demonstration here. What is of interest for us is the form of the linear representation of the generic vector $\bar{x}$ in terms of the eigenvectors $\bar{e}$. After defining the inner product between two vectors $\bar{x}$ and $\bar{y}$ of S:

$$(\bar{x}, \bar{y}) = \sum_{k=1}^{3N} x_k^* y_k \tag{8}$$

where x_k^* denotes the conjugate of the k-th component of $\bar{x}$, we observe that any vector $\bar{x}$ can be given the expression:

$$\bar{x} = \sum_{j=1}^{3N} (\bar{f}_j^*, \bar{x})\bar{e}_j \tag{9}$$

Here the inner products $(\bar{f}_j^*, \bar{x})$ are the coefficients of the linear superposition and can be accordingly interpreted as the components of $\bar{x}$ on the basis of the eigenvectors $\bar{e}_j$. The demonstration of the expression (9) is straightforward. From the equality $E^{-1}E = I$, and the definitions (5) and (6), it follows that the inner products between the vectors $\bar{f}^*$ and $\bar{e}$ have the values:

$$(\bar{f}_j^*, \bar{e}_k) = \delta_{jk} \quad 1 \le j, k \le 3N \tag{10}$$

where δ_{jk} is the Kronecker delta. In terms of vector algebra, this expression (10) states
that any vector $\bar{f}_j^*$ has a unitary component over the basis vector $\bar{e}_j$ and is orthogonal to
all the other basis vectors, namely it is orthogonal to the $3N-1$-dimensional subspace
described by the ensemble of vectors $\bar{e}_k, k \neq j$. Now, after writing

where δ_{jk} is the Kronecker delta. In terms of vector algebra, this expression (10) states that any vector $\bar{f}_j^*$ has a unitary component over the basis vector $\bar{e}_j$ and is orthogonal to all the other basis vectors, namely it is orthogonal to the $3N-1$-dimensional subspace described by the ensemble of vectors $\bar{e}_k, k \neq j$. Now, after writing

$$\bar{x} = \sum_{j=1}^{3N} A_j \bar{e}_j$$

(which is possible in virtue of the completeness of the eigenvectors basis), and after inner-multiplying both members of the above equality by $\bar{f}_j^*$, it can be shown with the aid of the eqs (10) that the complex coefficients A_j have just the form given in the expression (9).

The above premises having been posed, we can focus on the properties specifically related to the fact that the matrix C is real. A real matrix admits both real and complex eigenvalues, but if it admits the complex eigenvalue λ, it admits even the conjugate eigenvalue λ^*; moreover if $\bar{e}$ is the eigenvector corresponding to λ, hence that one corresponding to λ^* is $\bar{e}^*$. This follows immediately from the equality $C\bar{e} = \lambda\bar{e}$, since, after taking the conjugate of both members, the result is $C\bar{e}^* = \lambda^*\bar{e}^*$. As a consequence the complex eigenvalues and eigenvectors of C can be grouped in pairs of conjugate values, each pair describing a 2-dimensional subspace of S. Now, there is no loss of generality in assuming that $\bar{e}_j$ and $\bar{e}_{j+1}$ form one of such pairs, describing the subspace S_j, that is let us suppose that:

$$\bar{e}_{j+1} = \bar{e}_j^* \qquad \lambda_{j+1} = \lambda_j^* \tag{11}$$

Applying the eqs (10) to our case, we find that:

$$(\bar{f}_j^*, \bar{e}_j) = 1, \quad (\bar{f}_j^*, \bar{e}_j^*) = 0, \quad (\bar{f}_j^*, \bar{e}_k) = 0 \quad k \neq j \text{ and } j+1 \tag{12}$$

By taking the conjugate of all the above equalities we obtain that

$$(\bar{f}_j, \bar{e}_j^*) = 1, \quad (\bar{f}_j, \bar{e}_j) = 0, \quad (\bar{f}_j, \bar{e}_k^*) = 0 \quad k \neq j \text{ and } j+1 \tag{13}$$

which shows that the vector $\bar{f}_j$ has a unitary component over the eigenvector $\bar{e}_{j+1} = \bar{e}_j^*$ and is orthogonal to all other eigenvectors $\bar{e}$ of C and enables us to write:

$$\bar{f}_{j+1} = \bar{f}_j^* \tag{14}$$

Hence likewise λ and $\bar{e}$ even the vectors $\bar{f}$ can be grouped in pairs of conjugate values. Now, let us turn our attention to the solution of the wave propagation problem and let us examine the consequences of the above stated properties on the spectral representation given in (7). The first observation is that the wave propagator $P(t)$ is a real matrix that admits exactly the same eigenvectors as C and that has the eigenvalues $\exp(\lambda_j t)$. If we

restrict the discussion to the 2D subspace spanned by the pair of eigenvectors $\bar{e}_j$ and $\bar{e}_{j+1}$, the real vector describing the initial condition $\bar{\xi}_0$ can be given the representation:

$$(\bar{\xi}_0)_j = (\bar{f}_j^*, \bar{\xi}_0)\bar{e}_j + (\bar{f}_{j+1}^*, \bar{\xi}_0)\bar{e}_{j+1} = (\bar{f}_j^*, \bar{\xi}_0)\bar{e}_j + (\bar{f}_j, \bar{\xi}_0)\bar{e}_j^* = 2\Re\{(\bar{f}_j^*, \bar{\xi}_0)\bar{e}_j\} \qquad (15)$$

where $\Re\{\cdot\}$ denotes the real part of the complex number between braces. Herafter $\Im\{\cdot\}$ will be analogously used to designate the imaginary part. After introducing the real vectors:

$$\bar{\eta}_j = \Re\{\bar{e}_j\} \quad \bar{\chi}_j = \Im\{\bar{e}_j\} \qquad (16a)$$

and the real coefficients:

$$a_j = 2\,(\Re\{\bar{f}_j\}, \bar{\xi}_0), \quad b_j = -2\,(\Im\{\bar{f}_j\}, \bar{\xi}_0) \qquad (16b)$$

the representation (15) of $\bar{\xi}_0$ assumes the simple form:

$$(\bar{\xi}_0)_j = a_j \bar{\eta}_j + b_j \bar{\chi}_j \qquad (17)$$

If we apply $P(t)$ to such an initial condition we obtain the solution $(\bar{\xi})_j$ at the time t, that is:

$$(\bar{\xi})_j = (\bar{f}_j^*, \bar{\xi}_0)\bar{e}_j e^{\lambda_j t} + (\bar{f}_{j+1}^*, \bar{\xi}_0)\bar{e}_{j+1} e^{\lambda_{j+1} t})$$

After calling α and ω the real and imaginary part of the eigenvalue respectively, that is:

$$\lambda_j = \alpha_j + i\omega_j \qquad (18)$$

where i is here the imaginary unit, and after some calculations, the solution can be put in the form:

$$(\bar{\xi})_j = 2e^{\alpha_j t}\Re\{(\bar{f}_j^*, \bar{\xi}_0)\bar{e}_j e^{i\omega_j t}\} \qquad (19)$$

With the aid of the positions:

$$\bar{\rho}_j = 2\Re\{(\bar{f}_j^*, \bar{\xi}_0)\bar{e}_j\} = a_j \bar{\eta}_j + b_j \bar{\chi}_j = (\bar{\xi}_0)_j \qquad (20a)$$

$$\bar{\sigma}_j = -2\Im\{(\bar{f}_j^*, \bar{\xi}_0)\bar{e}_j\} = b_j \bar{\eta}_j - a_j \bar{\chi}_j \qquad (20b)$$

the expression (19) can be further simplified to:

$$(\bar{\xi})_j = e^{\alpha_j t}(\bar{\rho}_j \cos \omega_j t + \bar{\sigma}_j \sin \omega_j t) \qquad (21)$$

which is the representation we were looking for.

Let us now consider the case where the initial condition $\bar{\xi}_0$ has a nonvanishing component over the eigenvector $\bar{e}_k$ whose associated real eigenvalue is λ_k. First of all, it is convenient to demonstrate that the eigenvector $\bar{e}_k$ can be assumed to be a real vector. Let us suppose that $\bar{e}_k$ is complex. Hence from the equality $C\bar{e}_k = \lambda_k \bar{e}_k$, we deduce that both $\Re\{\bar{e}_k\}$ and $\Im\{\bar{e}_k\}$ satisfy the eigenvector equation associated with the same eigenvalue λ_k and consequently, if λ_k is a simple real eigenvalue, they have to be

linearly dependent. Accordingly, after posing $\Re\{\tilde{e}_k\} = \tilde{\varsigma}_k \cos\theta$ and $\Im\{\tilde{e}_k\} = \tilde{\varsigma}_k \sin\theta$, where $\theta = \arctan(\Im\{\tilde{e}_k\}/\Re\{\tilde{e}_k\})$, we conclude that the eigenvector can be written in the form $\tilde{e}_k = \tilde{\varsigma}_k \exp(i\theta)$. Here $\tilde{\varsigma}_k$ is a real vector satisfying the condition $|\tilde{\varsigma}_k| = 1$ in force of the normalization condition $|\tilde{e}_k| = 1$. Moreover, we notice that all the unit vectors we obtain from the above expression by taking an arbitrary value of θ, satisfy the eigenvalue equation and are therefore eigenvectors corresponding to λ_k. This ambiguity is not a problem and we will see that it is not peculiar of the eigenvectors associated with real eigenvalues, but regards all the eigenvectors, and will be dealt with at the end of this section. What matters here is that with no loss of generality we can assume $\theta = 0$, implying that the eigenvector $\tilde{e}_k$ corresponding to λ_k is real. Strictly speaking, the above demonstration has been performed under the hypothesis that λ_k is a simple eigenvalue, but it could be easily extended to covering the case of multiple real eigenvalues.

So far we have seen that the eigenvectors of C are either real or grouped in pairs of conjugate values. In the following we will thus assume that C admits p real eigenvectors and q pairs of conjugate eigenvectors, defining q 2D subspaces of the complex 3N-dimensional space S, with the trivial condition that $p+2q = 3N$. As an immediate result of this property, it can be stated that the vector basis formed by the conjugate vectors $\tilde{e}^*$ coincides with the eigenvector basis $\tilde{e}$, apart from the irrelevant vector numbering: indeed the conjugation does not change the p real eigenvectors, while simply interchanges the eigenvectors of the q pairs of conjugate values, mapping each of the q 2D subspaces onto itself. A further relevant point is that from $\tilde{e}_k$ being real descends that even $\tilde{f}_k$ must be real. This can be proven by assuming first that $\tilde{f}_k$ is complex. In light of the equations (10), taking the conjugate of both members, we deduce that $(\tilde{f}_k, \tilde{e}_k) = 1$ and that $(\tilde{f}_k, \tilde{e}_j^*) = 0$ when $(j \neq k)$. This means that the vector $\tilde{f}_k^*$ has a unitary component over $\tilde{e}_k$ and is orthogonal to all vectors $\tilde{e}_j^*$ $(j \neq k)$. But in virtue of the above stated identity of the vector bases $\tilde{e}$ and $\tilde{e}^*$, the vector $\tilde{f}_k^*$ results to be normal even to all the eigenvectors $\tilde{e}_j$ $(j \neq k)$. Therefore the eqs.(10) hold for both $\tilde{f}_k^*$ and $\tilde{f}_k$, which implies that $\tilde{f}_k^* = \tilde{f}_k$, an equation that can be fulfilled only if $\tilde{f}_k$ is a real vector.

After the previous considerations, we are able to write the image $(\tilde{\xi}_0)_k$ of the initial condition $\tilde{\xi}_0$ over the real eigenvector $\tilde{e}_k$, namely:

$$(\tilde{\xi}_0)_k = c_k \tilde{e}_k \quad c_k = (\tilde{f}_k, \tilde{\xi}_0) \tag{22}$$

where c_k is a real coefficient, resulting from the inner product of two real vectors. And if we pose:

$$\tilde{\psi}_k = c_k \tilde{e}_k = (\tilde{\xi}_0)_k \qquad \beta_k = \lambda_k \tag{23}$$

it is straightforward to infer that the expression of the corresponding solution at the time t is:

$$(\tilde{\xi})_k = e^{\beta_k t} \tilde{\psi}_k \tag{24}$$

Combining together the expressions (21) and (24) related respectively to the conjugate eigenvectors pairs and to the real eigenvectors, we can deduce the general form for the solution of the tsunami propagation problem:

$$\tilde{\xi}(t) = \sum_{j=1}^{q} e^{\alpha_j t}(\tilde{\rho}_j \cos \omega_j t + \tilde{\sigma}_j \sin \omega_j t) + \sum_{k=1}^{p} e^{\beta_k t} \tilde{\psi}_k \tag{25}$$

that at the time $t = 0$ reduces correctly to the initial condition:

$$\tilde{\xi}(0) = \sum_{j=1}^{q} \tilde{\rho}_j + \sum_{k=1}^{p} \tilde{\psi}_k = \tilde{\xi}_0 \tag{26}$$

the last equality descending from the positions (20) and (23). The solving expression (25) is the explicit translation of the formula (7) and proves that the solution can be computed in terms of exponential and circular time functions, as will be discussed later on.

Before concluding the present section, we will address the problem of the nonuniqueness of the eigenvectors in the complex space S, that we have only grazed in the above treatment. We observe that, given an eigenvector $\tilde{e}_j$, all the vectors resulting from multiplying $\tilde{e}_j$ by a complex constant of unitary norm are eigenvectors corresponding to the same eigenvalue λ_j since they satisfy both the eigenvalue equation and the normalization condition given in (5). This ambiguity can be formulated by saying that any eigenvector $\tilde{e}_j$ is uniquely determined apart from an arbitrary complex constant $\mu_j = \exp(i\theta_j)$. It is important to emphasize that the choice of these arbitrary constants has no effect on the final solution (25). Indeed, let us consider the new eigenvector basis $\tilde{e}'$, where $\tilde{e}'_j = \mu_j \tilde{e}_j$. Firstly, from the eqs (10) it is easy to deduce that $(\tilde{f}'_j)^* = \mu_j \tilde{f}_j^*$. Hence the component x'_j of the generic vector $\tilde{x}$ over the eigenvector $\tilde{e}'_j$ is given by $x'_j = (\tilde{f}'^*_j, \tilde{x}) = \mu_j^*(\tilde{f}_j^*, \tilde{x}) = \mu_j^* x_j$. If we apply the above findings to the equations (22) and (23) concerning the real eigenvalues, we obtain first that $c'_k = \mu_k^* c_k$ and then that $\tilde{\psi}'_k = \tilde{\psi}_k$, which entails that the eq (24) holds regardless the choice of the constant μ. Less immediate is to reach the same conclusion for the nonreal eigenvalues, since the choice of the constants μ_j and μ_{j+1} can break the conjugation relationship between the j-th and the $j + 1$-th eigenvectors. Let us then suppose that:

$$\tilde{e}'_j = \mu_j \tilde{e}_j \quad \tilde{e}'_{j+1} = \nu_j \mu_j^* \tilde{e}_{j+1} \quad |\mu_j| = |\nu_j| = 1 \tag{27a}$$

entailing also that:

$$\tilde{f}'^*_j = \mu_j \tilde{f}_j^* \quad \tilde{f}'^*_{j+1} = \nu_j \mu_j^* \tilde{f}_{j+1}^* \tag{27b}$$

and let us write the expression corresponding to the equation (15) in terms of the new eigenvectors:

$$(\tilde{\xi}_0)_j = (\tilde{f}'^*_j, \tilde{\xi}_0)\tilde{e}'_j + (\tilde{f}'^*_{j+1}, \tilde{\xi}_0)\tilde{e}'_{j+1} \tag{28}$$

The relation between the eigenvector $\tilde{e}'_{j+1}$ and $\tilde{e}'_j{}^*$ can be found to be:

$$\tilde{e}'_{j+1} = \nu_j \mu_j^* \tilde{e}_{j+1} = \nu_j \mu_j^* \tilde{e}_j^* = \nu_j \tilde{e}'_j{}^* \tag{29}$$

where the first and the third equalities derive from the eqs.(27a), whereas the second equality is a consequence of the relations (11). Analogously, it can be proven that the relationships between $\tilde{f}'_{j+1}{}^*$ and $\tilde{f}'_j$ is:

$$\tilde{f}'^*{}_{j+1} = \nu_j \mu_j^* \tilde{f}_{j+1}^* = \nu_j \mu_j^* \tilde{f}_j = \nu_j \tilde{f}'_j \tag{30}$$

In the above chain of equalities, the first and the third ones can be justified basing on the relationships (27b), while the second results from the equations (14). If we make use of the equations (29) and (30), the expression (28) can be rewritten as:

$$(\tilde{\xi}_0)_j = (\tilde{f}'_j{}^*, \tilde{\xi}_0)\tilde{e}'_j + (\tilde{f}'_j, \tilde{\xi}_0)\tilde{e}'_j{}^* = 2\Re\{(\tilde{f}'^*{}_j, \tilde{\xi}_0)\tilde{e}'_j\} \tag{31}$$

that is formally equal to the expression (15), though in terms of the new *primed* vectors. If we introduce definitions for the vectors $\tilde{\eta}'_j$ and $\tilde{\chi}'_j$ and for the coefficients a'_j and b'_j that are analogous to those given in (16a) and (16b), that is:

$$\tilde{\eta}'_j = \Re\{\tilde{e}'_j\} \quad \tilde{\chi}'_j = \Im\{\tilde{e}'_j\} \tag{32a}$$

$$a'_j = 2\,(\Re\{\tilde{f}'_j\}, \tilde{\xi}_0), \quad b'_j = -2\,(\Im\{\tilde{f}'_j\}, \tilde{\xi}_0) \tag{32b}$$

After recalling that $(\tilde{f}'^*{}_j, \tilde{\xi}_0) = \mu^*(\tilde{f}_j^*, \tilde{\xi}_0)$, we can easily obtain the relationships between the vectors:

$$\tilde{\eta}'_j = \tilde{\eta}_j \cos\theta_j - \tilde{\chi}_j \sin\theta_j \quad \tilde{\chi}'_j = \tilde{\eta}_j \sin\theta_j + \tilde{\chi}_j \cos\theta_j \tag{33}$$

and between the coefficients:

$$a'_j = a_j \cos\theta_j - b_j \sin\theta_j \quad b'_j = a_j \sin\theta_j + b_j \cos\theta_j \tag{34}$$

where we have posed that $\cos\theta_j$ and $\sin\theta_j$ are respectively the real and the imaginary part of the complex unit-norm coefficient μ_j. Repeating the steps that led us to the expression (19) for the solution $(\tilde{\xi}_j)$, we can now write the analogous formula:

$$(\tilde{\xi})_j = 2e^{\alpha_j t}\,\Re\{(\tilde{f}'^*{}_j, \tilde{\xi}_0)\,\tilde{e}'_j\,e^{i\omega_j t}\} \tag{35}$$

Since, with the aid of the relationships (33) and (34), it is easy to verify that

$$a'_j \tilde{\eta}'_j + b'_j \tilde{\chi}'_j = a_j \tilde{\eta}_j + b_j \tilde{\chi}_j \quad b'_j \tilde{\eta}'_j - a'_j \tilde{\chi}'_j = b_j \tilde{\eta}_j - a_j \tilde{\chi}_j$$

we come to the important conclusion that the representation (21) does not depend upon the arbitrary constants μ_j and μ_{j+1}. The extension of this invariance property to the general representation (25) is the trivial further step that concludes our demonstration.

On the basis of the proven invariance we will refer to the representation (21) and (24) respectively as the one concerning the complex conjugate eigenvectors and the real eigenvectors of C, though we know that the former may be not conjugate and the latter may be not real.

Discussion and Conclusions

The general representation (25) of the solution to the tsunami propagation problem espresses the vector field $\tilde{\xi}(t)$ at the time t as the linear combination or superposition of time-independent real vectors (namely $\tilde{\rho}_j$ and $\tilde{\sigma}_j$, $j = 1, ..., q$, and $\tilde{\psi}_k$, $k = 1, ..., p$) weighted by simple real time functions (exponential and circular functions) determined by real constants with dimension $1/t$: α_j and ω_j, $j = 1, ..., q$, and β_k, $k = 1, ..., p$. In light of the definitions (20a), (20b) and (23), the real vectors depend in turn on the real coefficients a_j, b_j and c_k as well as on the real and imaginary parts of the conjugate eigenvectors $\bar{\eta}_j$ and $\bar{\chi}_j$, and on the real eigenvectors $\bar{e}_k$. Notice that the vectors $\bar{\eta}_j$ and $\bar{\chi}_j$, being independent linear superpositions of the eigenvectors $\bar{e}_j$ and $\bar{e}_{j+1}$, belong entirely to the 2D subspace S_j. Observe further that the initial condition $\tilde{\xi}_0$ influences solely the $3N$ coefficients a_j, b_j and c_k, but it has no effect either on the above quoted vectors or on the parameters in the time functions, for they are uniquely determined by the spectral decomposition of the matrix C: this means that they convey information on the basic governing equations and on the geometrical features of the grid (here including both triangulation and basin bathymetry).

Let us now consider separately the behaviour of the components corresponding to a real eigenmode and to a pair of conjugate eigenmodes. In the former case the elementary representation (24) says that the solution persists over the initial vector $\tilde{\psi}_k$, that is proportional to the eigenmode $\bar{e}_k$, with an amplitude changing exponentially with time according to the characteristic time $\tau_k = 1/|\beta_k|$. The mode either decays ($\beta_k < 0$) or grows ($\beta_k > 0$) indefinitely, tending asymptotically either to be vanishing or to diverge. Since this component is constrained to remain in the same eigenmode, as a matter of fact it represents a stationary wave for the grid: crests and troughs cannot move staying in their respective initial positions, zero-elevation nodes and zero-velocity nodes rest in their null state at any time, and the global field pattern remains unchanged, while the wave amplitude becomes larger or smaller. The above observation regarding a single component does not imply that even a linear combination of vectors of this type is a stationary wave. In fact the total wave pattern is determined by the mutual weights of the single interfering components, that in turn depend on time according to the related exponentials $\exp(\beta_k t)$. For example, let us suppose that at a certain time t' two components k and l are exactly in balance over a given grid node m, that is $c_k(\bar{e}_k)_m \exp(\beta_k t') + c_l(\bar{e}_l)_m \exp(\beta_l t') = 0$. Now, if $\beta_k \neq \beta_l$, it follows that at any time $t \neq t'$, the interference between the two considered components differs from

zero over that node. Therefore, in general it can be stated that positive-valued, zero-valued and negative-valued regions are not stable field features of the real eigenmode representation. A special comment deserves the case of $\beta_k = 0$, corresponding to the case of a null eigenvalue $\lambda_k = 0$. This entails that the solution persists on the eigenmode $\bar{e}_k$ with magnitude c_k, so that the component reduces to the steady state $\bar{\psi}_k$. It is easy to see that if $\lambda_k = 0$ is an eigenvalue with multiplicity n, the superposition of the n components corresponding to the n distinct null eigenmodes turns out to be a steady state absolutely independent from time.

Let us turn our attention to the behaviour of the components corresponding to the pairs of conjugate eigenmodes, a behaviour which is the result of a periodic evolution with circular frequency ω_j and period $T_j = 2\pi/\omega_j$, and of an exponential that describes a time decay or growth depending on the constant α_j being negative or positive. The main difference from the previous case is that the solution passes continuously from the initial state $\bar{\rho}_j$ to the linearly independent state $\bar{\sigma}_j$, and then to the respective opposite states $-\bar{\rho}_j$ and $-\bar{\sigma}_j$ that are attained each fourth of period T_j. At any cycle the component repeats its state, but with different amplitude according to the exponential law, and in the special case where $\alpha_k = 0$, the motion is purely periodic. It is clear that the wave pattern cannot be stationary, since it transforms cyclically from that pertaining to the state $\bar{\rho}_j$ to that associated with $\bar{\sigma}_j$: therefore these components of the solution, being intrinsically evolutive, are particularly suited to describe travelling waves.

The representation (25) can be interpreted as the spectral decomposition of the solution, for it is a linear superposition of vectors that are either eigenvectors or simply related to the eigenvectors. Since the eigenvectors and all the parameters in the time laws in the expression (25) depend on the grid geometry and on the space discretization technique used for the hydrodynamic equations (1), it would be quite important to understand the nature of such a dependence. In fact, for example, if we knew something more about the influence of the grid on the eigenmodes of C, we would use this knowledge as a guidance to devise an optimal gridding algorithm, providing that mesh that is best suited to the problem. In a previous paper (Tinti et al., 1996) some general properties of invariance under some classes of transformations such as variable scaling and grid rotation were shown to hold for the eigenvalues and the eigenvectors of the matrix C. But this is still insufficient to provide a good criterion for the grid selection. More useful in this respect is the observation that the shortest of the eigenmode periods T_j is found to be comparable with the shortest crossing time of the grid elements, which poses a strict relationships between the highest frequency compatible with the system, that is the time resolution, and the size of the smallest grid element, that is the space resolution. It is clear, however, that more research is needed in order to have a better insight on the relationships between the grid characteristics (i.e. element type, number of nodes, heterogeneity) and the hydrodynamic equations (for instance the boundary conditions) on one side and the resulting eigenmodes and eigenvalues of the spectral decomposition on the other side, which will be the object of future investigations.

Acknowledgments

References

Tinti S. and Piatanesi A., 1995, Wave propagator in finite-element modeling of tsunamis, *Marine Geodesy*, 18, 273–298.

Tinti S., Piatanesi A. and Bortolucci E., 1996, On some properties of the FE tsunami "Wave Propagator", *Science of Tsunami Hazards* (in press).

PROPAGATION AND RUNUP OF TSUNAMI WAVES GENERATED BY MT. ST. AUGUSTINE VOLCANO, ALASKA

Jurgen Kienle, Zygmunt Kowalik and Elena Troshina

Institute of Marine Science
and Geophysical Institute
University of Alaska Fairbanks
Fairbanks, AK 99775

ABSTRACT

The eruption of Mt. St. Augustine Volcano, Alaska, in 1883 resulted in a landslide which produced tsunami of about 6 m high at English Bay, 85 km east of Augustine Island. This study uses numerical modeling to forecast the tsunami waves which may be generated by future eruptions. The numerical model is based on the nonlinear shallow-water equations which are solved by a finite-difference method. The simulation yields runup heights and inundation patterns. Two landslides are considered for investigation of how different source parameters influence tsunami travel times and runup heights. This study uses four embedded interactive numerical grids for Lower Cook Inlet to propagate a tsunami signal from Mt. St. Augustine Volcano to the shores and to compute the runup heights for Homer and English Bay. The results of numerical modeling allow evaluation of the potential tsunami hazard for Lower Cook Inlet.

I. INTRODUCTION.

Tsunamis of volcanic origin are rarely observed but are known to be violent and destructive (Lander and Lockridge, 1989). The area examined in this study includes Cook Inlet, a 300 km long, 30-100 km wide estuary in southern Alaska. A number of communities is located along the eastern shore of Cook Inlet. There are five active volcanoes on its western, mostly uninhabited, shore. Two of them have generated debris flows, that reached the sea: Redoubt, 3 times in Holocene time (Begét and Nye, 1994), and Augustine, 12 times in the past 2000 years (Begét and Kienle, 1992). The last Augustine debris avalanche, on October 6, 1883 generated tsunami of about 6 m high at English Bay, 85 km to the east of the volcano across the Inlet (Kienle *et al.*, 1987).

This work is an extension of a previous study dealing with tsunami generated by edifice collapse of Mt. St. Augustine Volcano (Kienle *et al.*, 1987). The authors developed the numerical model to include Lower Cook Inlet from 59^0N to about 60^0N (Figure 1). The model did not simulate runup which locally could amplify wave height because the variable depth and shoreline generate local differences in amplitude and velocity of the wave that cannot be resolved by the numerical grid used for the wave propagation. To properly model all these phenomena, the described Mt. St. Augustine tsunami model is improved by introducing four embedded grids for Lower Cook Inlet (Troshina, 1996). This approach allows a tsunami wave to propagate from Augustine Island to the Cook Inlet shorelines with ever-increasing resolution (from 926 m grid spacing to 20.6 m grid spacing) as the wave approaches the coast. The domain with the shortest grid spacing includes both sea bottom and land topography allowing a smooth propagation of the tsunami wave from wet to dry regions.

II. MODEL.

The following set of shallow-water equations of motion and continuity is used in this study (Kowalik and Murty, 1993):

$$\frac{\partial u}{\partial t} + u\frac{\partial u}{\partial x} + v\frac{\partial u}{\partial y} - fv = -g\frac{\partial \zeta}{\partial x} - \frac{rWu}{D}, \tag{1}$$

$$\frac{\partial v}{\partial t} + u\frac{\partial v}{\partial x} + v\frac{\partial v}{\partial y} + fu = -g\frac{\partial \zeta}{\partial y} - \frac{rWv}{D}, \tag{2}$$

$$\frac{\partial \zeta}{\partial t} = \frac{\partial \eta}{\partial t} - \frac{\partial (Du)}{\partial x} - \frac{\partial (Dv)}{\partial y}. \tag{3}$$

Here u and v are the east-west (x) and north-south (y) components of velocity, respectively, g is gravity, f is the Coriolis parameter, ζ is the displacement of the free surface from the equilibrium level, η is the bottom displacement, $H(x,y)$ is the water depth in the equilibrium state, $D = H(x,y) + \zeta$ is the total depth, $W = \sqrt{u^2 + v^2}$, and r is the bottom friction coefficient.

At all shores, except for two small regions chosen for the runup calculations, the normal velocity component is assumed to be zero. As for the open boundary conditions, it is assumed that the wave processes occurring inside the numerical domain are not influenced
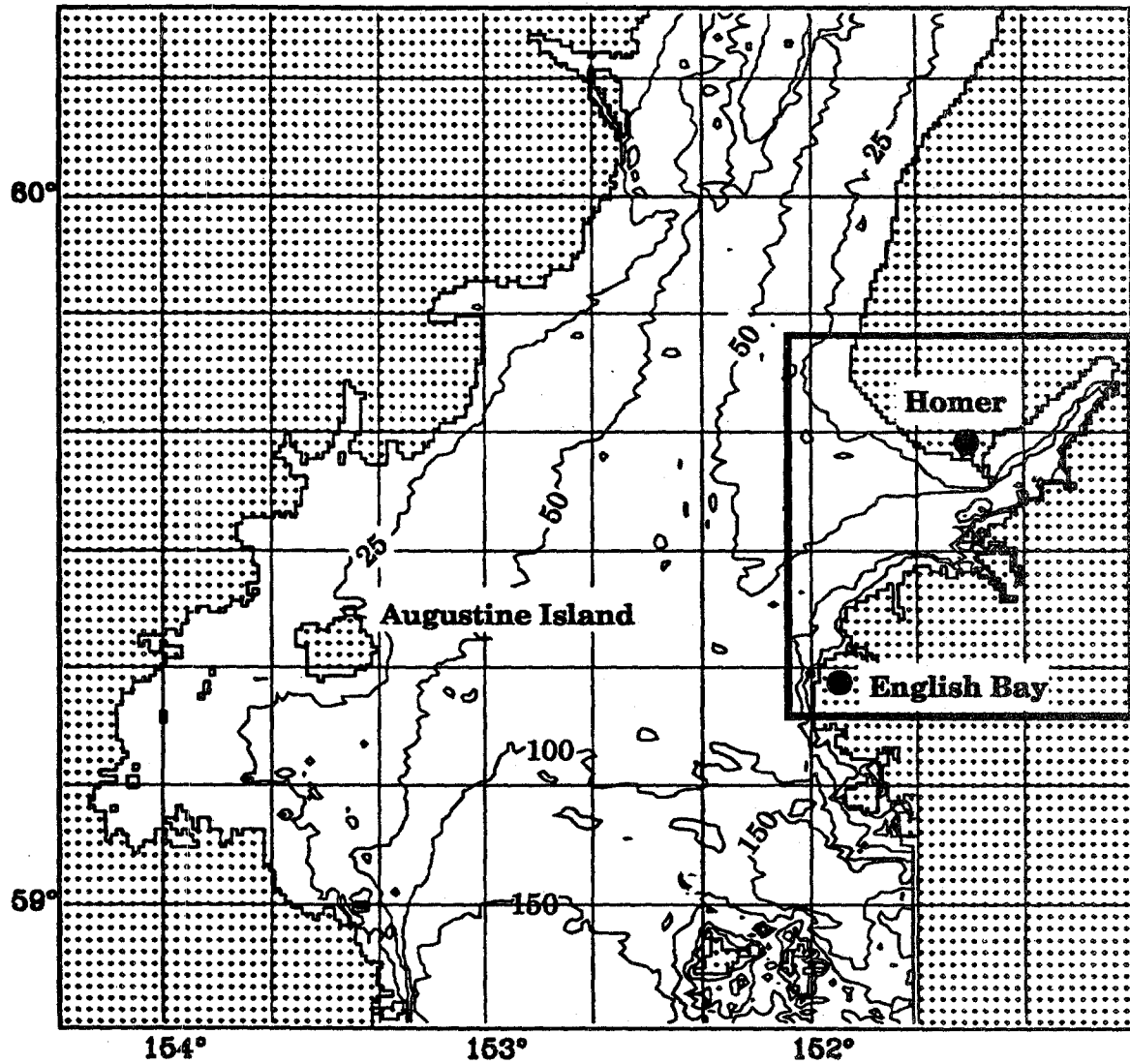
Figure 1. Lower Cook Inlet coarse grid of 927 m resolution. The area inside the frame is covered by the grid of 309 m resolution. Bathymetry contours show depth distribution in meters.

by the processes from outside, therefore the radiation condition given by Reid and Bodine (1968) is used.

To construct a numerical scheme, a space staggered grid is applied which requires either sea level or velocity as a boundary condition. The first order scheme is applied in time and in space. Integration is performed along the x and y directions separately. For this purpose the set (1)–(3) is split in time into two subsets. Denoting m as an index of numerical integration in time, the method can be explained through the following difference–differential equations.

First, these equations are solved along the x direction,

$$\frac{u^{m+1} - u^m}{T} + (u\frac{\partial u}{\partial x})^m + (v\frac{\partial u}{\partial y})^m = -g(\frac{\partial \zeta}{\partial x})^m - (\frac{ru\sqrt{u^2 + v^2}}{D})^m \qquad (4a)$$

$$\frac{1}{2}\frac{\zeta^* - \zeta^m}{0.5T} = -\frac{\partial(D^m u^{m+1})}{\partial x} \qquad (4b)$$

and next, along the y direction,

$$\frac{v^{m+1} - v^m}{T} + (v\frac{\partial v}{\partial y})^m + (u\frac{\partial v}{\partial x})^m = -g(\frac{\partial \zeta}{\partial y})^m - (\frac{rv\sqrt{u^2 + v^2}}{D})^m \qquad (5a)$$

$$\frac{1}{2}\frac{\zeta^{m+1} - \zeta^*}{0.5T} = -\frac{\partial(D^m v^{m+1})}{\partial y} \qquad (5b)$$

In this algorithm the calculation of the sea level starts from time step m, and along the x direction a preliminary value ζ^* is obtained. Afterwards, this value is carried over to the y direction to derive the sea level at the $m + 1$ time step.
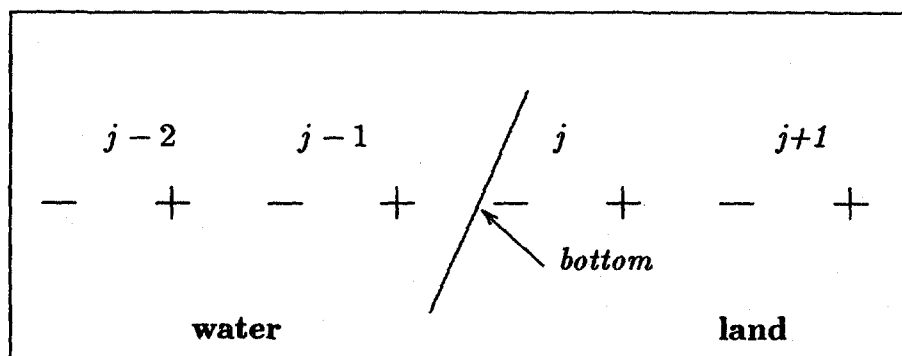

Fig. 2
Grid distribution for the run-up problem. Crosses denote sea level
grid points and dashes are velocity grid points.

To apply the boundary conditions at the water–land boundary, first, the boundary must be located at each time step. This is done by a simple algorithm proposed by Flather and Heaps (1975) for the tide computations and explained in Figure 2 for the x direction

only. To ascertain whether u_j is a dry or wet point (see Figure 2), the sea level is tested at this point;

$$\begin{cases} u_j \text{ is wet point} & \text{if } 0.5(D_{j-1} + D_j) \geq 0 \\ u_j \text{ is dry point} & \text{if } 0.5(D_{j-1} + D_j) < 0 \end{cases} \qquad (6)$$

It is obvious that the total depth is positive at the wet points and is equal to zero at the boundary because here $\zeta = -H$. The small negative value of the total depth set at the dry points allows to identify the location of all dry regions in the computational process. Next, Sielecki and Wurtele's (1970) extrapolation of the sea level to the first dry point is used. The velocity in the first dry point is extrapolated linearly from the two last points.

Realistic motion often takes place over discontinuous bathymetry where above simple extrapolation scheme for the moving boundary fails to reproduce the right answer. To account for the various cases of overtopped, submerged or exposed barriers, special boundary condition have been introduced based on the formulas for a submerged weir given by Reid and Bodine (1968). The above finite-difference runup numerical scheme is a modification of the scheme constructed by Kowalik and Murty (1993). The movement of the boundary follows from the equation of continuity, written for the upwind-downwind form, suggested by Mader (1988).

Two possible scenarios are modeled: 1) a landslide entering the sea at the northern shore of Augustine Island as in 1883 and 2) a landslide entering the sea at the volcano's eastern shore that faces Homer. One of the goals of this study is to evaluate the potential tsunami risk for the Homer Spit. For model calibration, the tsunami runup at English Bay is simulated for the case of the 1883 northern impact and computed wave heights are compared with available historical data. Afterwards, the runup heights are computed at the Homer Spit for both possible cases of landslide. Tsunamis generated in Cook Inlet propagate through a body of water that is already oscillating due to tides. In this study, tsunami waves arriving at coastal locations are considered at both low and high tides. This provides a more realistic assessment of the inundation which could be caused by tsunamis.

III. SOURCE MECHANISM.

The volcanic tsunamis can occur by submarine explosive activity, but more commonly they occur due to the entrance of debris avalanches or debris flows (landslides) into the sea. Numerous historical records gathered by Lander and Lockridge (1989) demonstrate the generation of very large water waves by landslides. Various mechanisms of transferring energy from the landslide into a tsunami have been tested through analytical solutions as well as through hydraulic and numerical modeling (Aida, 1969; Imamura and Imteaz, 1995; Kajiura, 1963; LeBlond and Jones, 1995; Noda, 1970; Wiegel, 1955).

The Augustine tsunami source model is constructed using the technique of the moving rigid bottom deformation. This motion is transmitted into the water column through the continuity of volume. Two scenarios of debris avalanche generation are studied. In the first, the landslide is assumed to enter the sea at Burr Point at the northern shore of Augustine Island, as in 1883. The area of the 1883 slide is computed to be 25 km^2 from a bathymetric map. The advance of the avalanche along the sea floor is simulated as a progressive 25-m high uplift of the sea floor, propagating from the shore to the open sea
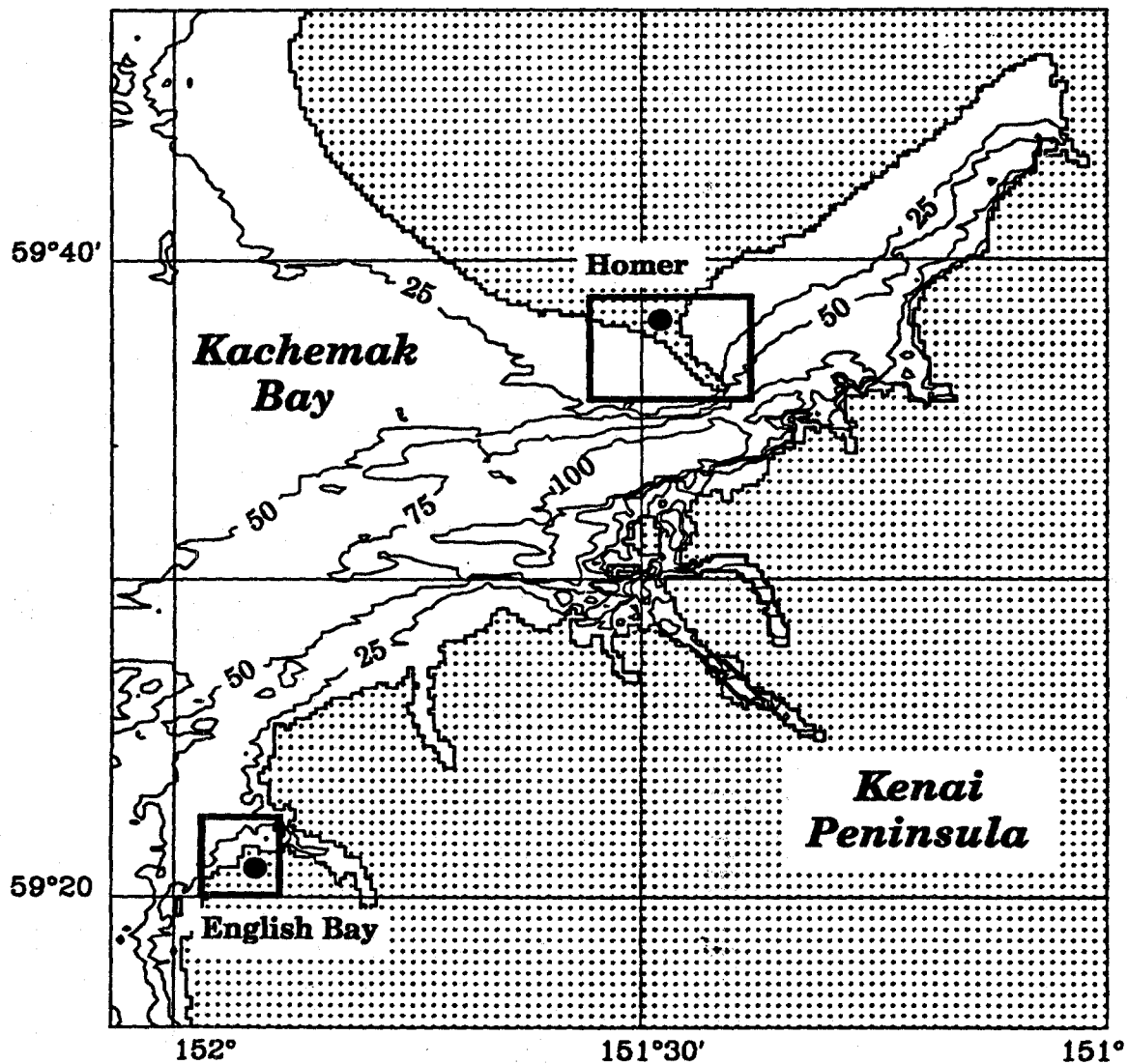
Figure 3. Kachemak Bay grid of 309 m resolution. The regions inside the two frames are finer grids of 61.8 m resolution. Bathymetry contours show depth distribution in meters.
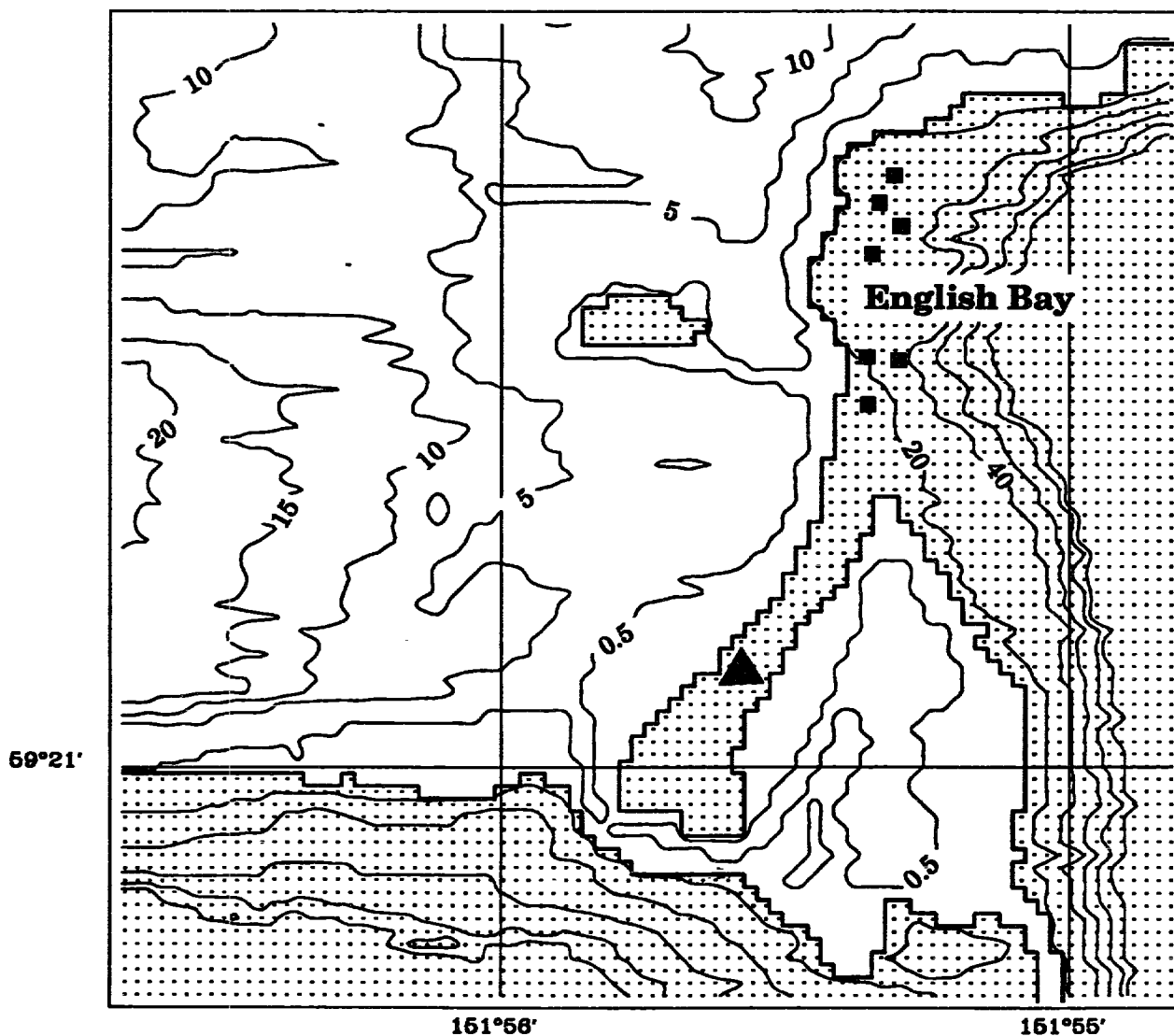
Figure 4. The grid of 20.6 m resolution for runup calculations at English Bay. Water depth and surrounding land elevations are in meters. The triangular mark indicates the location of the Alaska Commercial Company trading post in 1883; the squares show schematically the locations of buildings.
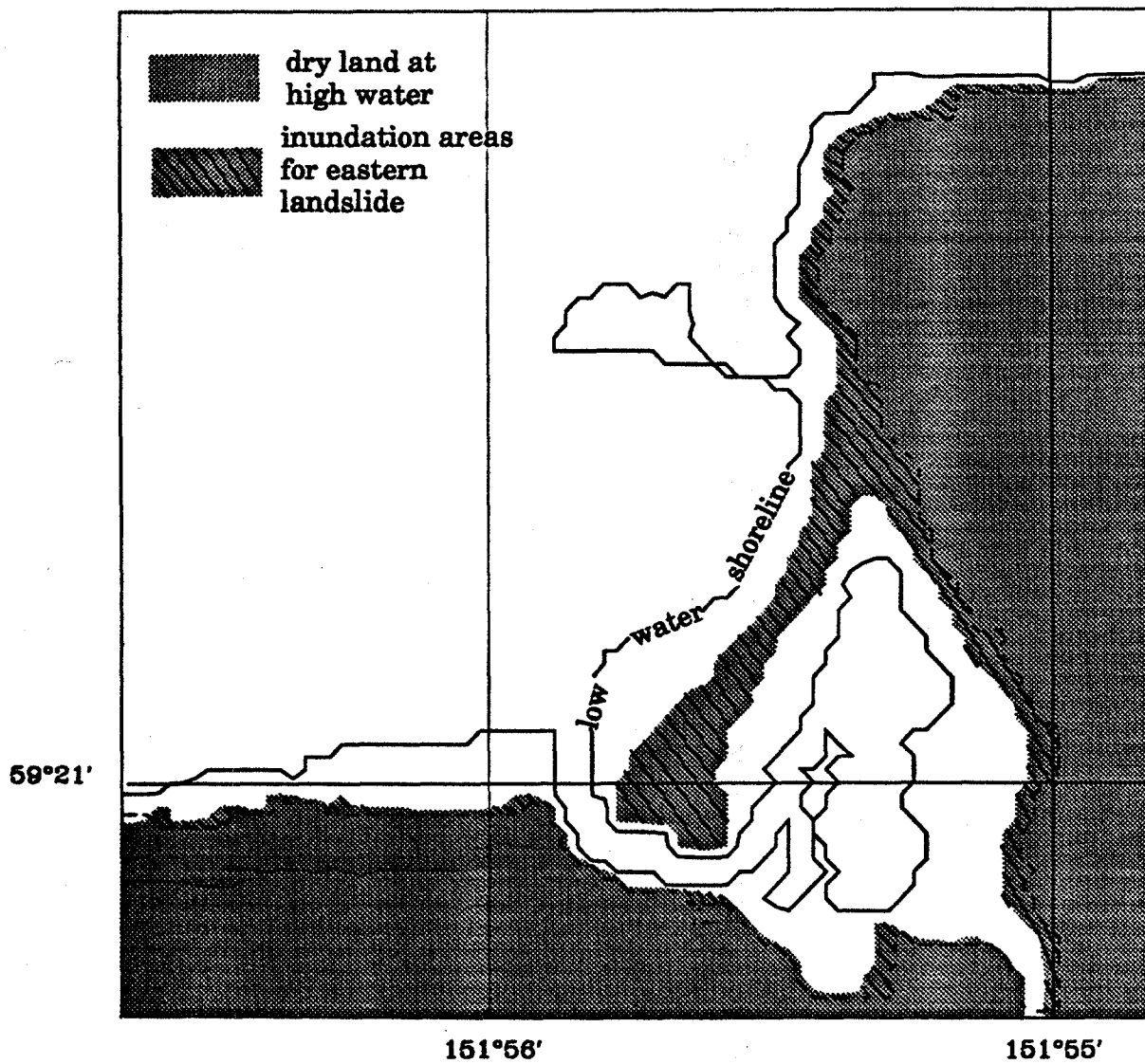
Figure 5. Tsunami inundation areas at English Bay for high tide conditions. Grey represents dry land at high tide, the hatched regions indicate areas inundated at high tide by tsunami generated at the eastern shore of Augustine Island.

at a speed of 50 m/s (Kienle *et al.*, 1987). In the second scenario, the debris avalanche is assumed to enter the sea at the eastern shore of the island where several prehistoric debris avalanches have been mapped offshore (Begét and Kienle, 1992). This model uses two main parameters of the landslide: its volume and its velocity.

IV. NUMERICAL GRIDS.

The region examined in this study extends from $59^0 50'$N to $60^0 16'$N and from 151^0W to $154^0 18'$W in south-central Alaska (Figure 1). This area, Lower Cook Inlet, includes all the coastal communities that might be threatened by a tsunami from Mt. St. Augustine. This research focuses on the village of English Bay, which was affected by the historic tsunami of 1883, and on the port of Homer, a location of interest to the fishing and tourist industry. The largest grid (Figure 1), with a resolution of 927 meters, covers Lower Cook Inlet. This coarse grid has a spacing of 1 minute in the longitudinal direction and 0.5 minute in the latitudinal direction. The coarse grid is coupled with a finer grid that covers the shallow coastal areas of Kachemak Bay from $59^0 16'$N to $59^0 48'$N and from 151^0W to $152^0 04'$W (Figures 1,3). The fine grid's resolution is one third that of the coarse grid, i. e., 309 meters. Two finer grids, of 61.8 meters resolution, are embedded into the Kachemak Bay grid (Figure 3). Each of them includes a final grid, with a horizontal space resolution of 20.6 meters, where the tsunami signal is finally resolved with a superfine runup model. Two regions of interest are:

1) English Bay (now Nanwalek). Here the grid of 61.8 meters resolution covers the shallow water of about 20 meters depth. The area chosen for runup calculations is shown in Figure 4. The superfine grid with 20.6 meters spacing covers about 1 square mile, half of which is covered with water. Coastal waters are very shallow including an intertidal lagoon adjacent to the village.

2) The Homer Spit in Kachemak Bay. Here again the grid of 61.8 meters resolution is used first. The superfine grid of 20.6 meters resolution, which covers the tip of the Homer Spit, serves for runup calculations (Figure 6). It includes the entrance to the Homer Harbor that would be exposed to potential tsunami waves.

Interactive connections are used between all pairs of grids which means that the wave passes through the boundary not only from the coarse-grid domain to the fine-grid domain but in the opposite direction as well. Such a detailed approach is important at English Bay and at the Homer Spit, both areas of complex bathymetry with entrances connecting local bays and harbors to the open waters.

V. RESULTS OF RUNUP COMPUTATIONS.

1. English Bay.

The village of English Bay on the southern Kenai Peninsula faces Cook Inlet and Mt. St. Augustine Volcano (Figures 1 and 4). The average elevation of the village is about 15 meters above mean sea level, and the elevation of the sand spit is about 5 meters. All houses are located at the foot of a 560-meter-high hill. The part of the village adjacent to
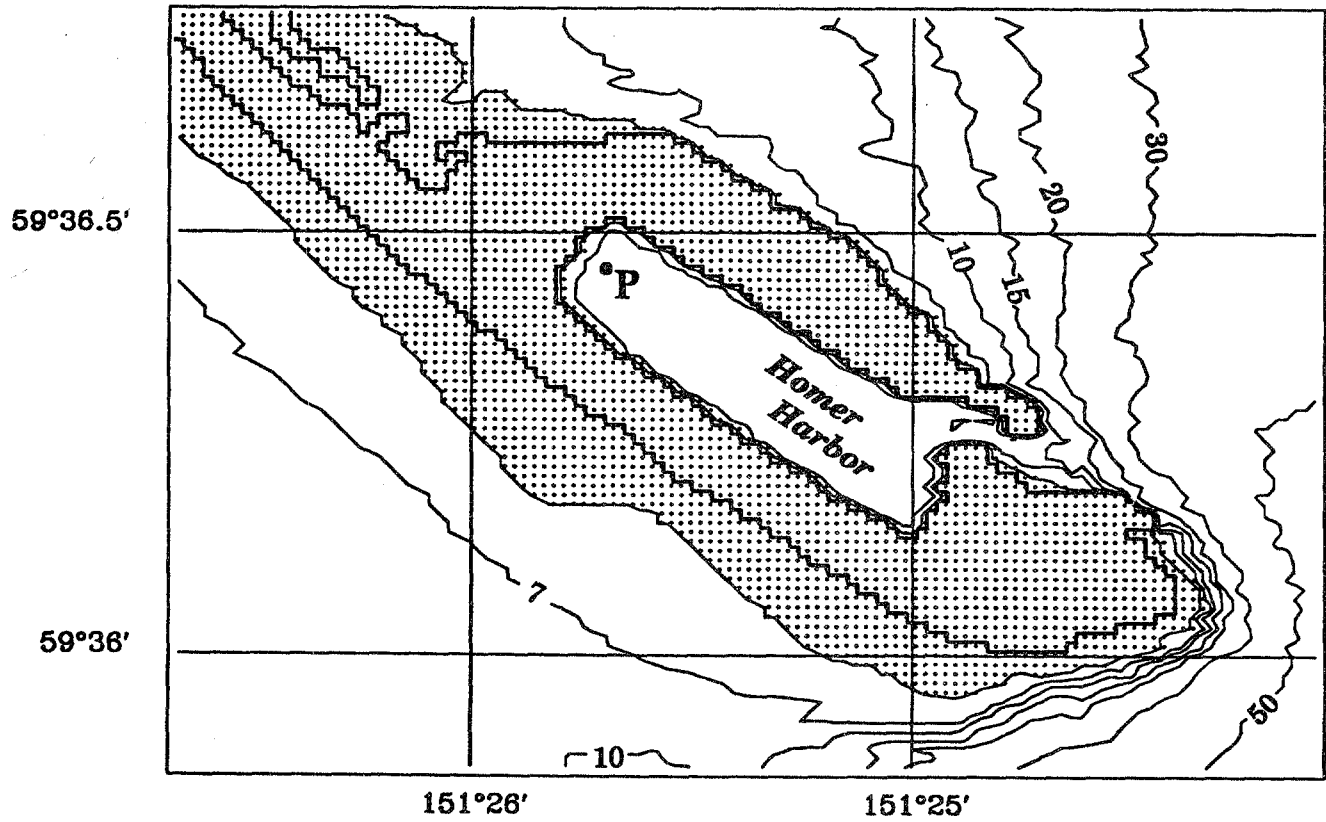
Figure 6. Runup grid of 20.6 m resolution for the tip of the Homer Spit. Water depth is in meters. The dotted area is dry land at low tide, the contour on the ground represents the shoreline at high tide. The point "P" indicates the location where sea level shown in Figure 8 was computed.
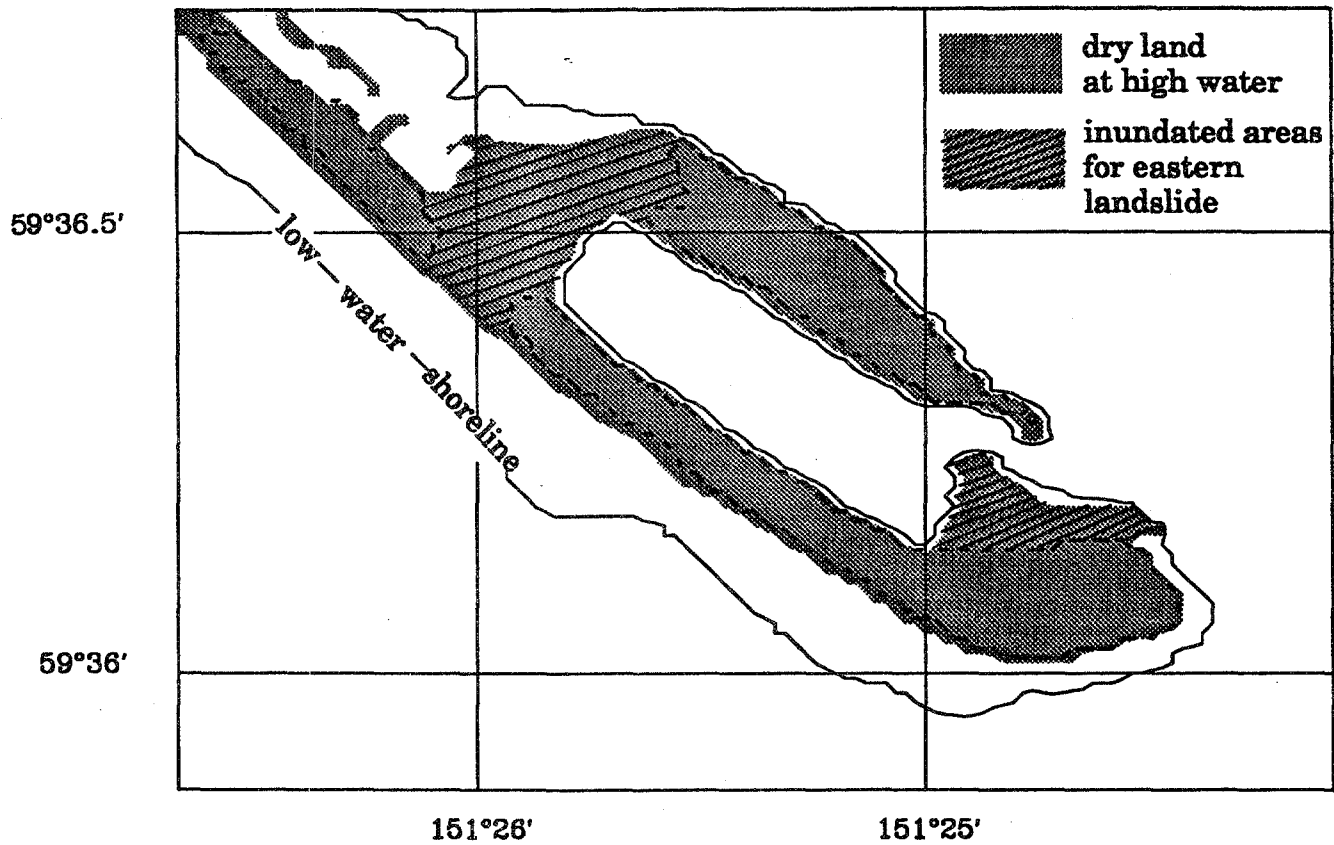
Figure 7. Tsunami inundation areas of the Homer Spit for high tide conditions. Grey represents dry land at high tide, the hatched regions indicate areas inundated at high tide by tsunami generated at the eastern shore of Augustine Island.

the entrance to the sand spit has the lowest elevation. For simulation of the 1883 event at English Bay, a very detailed grid is constructed to take into account the shoaling of the sea floor adjacent to the village, where the wavelength of the tsunami becomes shorter. Two bathymetric charts are generated for the runup calculations: one of them is for low tide, which corresponds to the 1883 event conditions, the other is for high tide. The average tidal range at English Bay is about 4.4 meters. Figure 4 shows the water depth and surrounding land elevations for the mean high water.

At time $t = t^*$ a tsunami wave with an amplitude of $A = A^*$ enters the western boundary of the superfine grid. Time t^* and amplitude A^* depend on the direction of the landslide (northern/eastern) and on the tide conditions (high water/low water); the average values are $t^* = 45$ min and $A^* = 1.5$ m. The period of the incoming wave is about 20 minutes. Calculations of runup are performed for both landslide scenarios as well as for two different stages of the tide, i.e. mean low water and mean high water.

Figure 5 represents tsunami inundation areas for an eastern landslide at high tide, which is the worst possible scenario. The area shown in gray is dry land at high tide; the hatched regions indicate areas flooded by tsunami waves. There are no dry spots on the spit when the waves are generated by the eastern landslide. At the spit, maximum runup heights at high water are 7.4 meters for the northern landslide and 9.4 meters for the eastern landslide with respect to mean low water level.

2. The Homer Spit.

The Homer Spit is a narrow glacial feature extending approximately 7.2 km from the town of Homer into Kachemak Bay (Figures 1 and 3). Homer (population 4,000) is the largest of the Lower Cook Inlet coastal communities; its low-lying glacial spit enjoys heavy summer recreational use and is especially vulnerable to large sea waves. The Port of Homer is located at the southeastern end of the spit. The Homer small boat harbor is home to 400 vessels; however, that number increases to 2,000 during the summer. The harbor basin depth varies from 4-6 meters at the southeast end to 3-5 meters at the northwest end. There is a single roadway on the Homer Spit that follows the crest of the spit, the average elevation of the road is about 9 meters with respect to mean low water.

The site chosen for runup calculations includes the very tip of the Homer Spit, where the Port of Homer is located. The area covered by the superfine runup grid of 20.6 m resolution (Figure 6) is about 3.8 square km. The dotted region in Figure 6 represents dry land at low tide, while the thick contour is the approximated shoreline for high tide condition. The mean tidal range is about 4.8 meters at the Homer Spit. Bathymetry contours radiate from the tip of the Homer Spit which results in strong wave refraction around it. Figure 7 shows inundation areas computed for the tip of the spit in the superfine grid with runup boundary conditions for an eastern landslide at high water. The area shown in gray represents dry land at high tide; the hatched regions are tsunami inundated areas. The area at the entrance to the harbor and the region adjacent to the southwest end of the harbor are completely flooded. Maximum runup heights occurring at high tide are 5.5 m for the northern landslide and 5.8 m for the eastern landslide with respect to mean low water level.

The plot in Figure 8 show sea level at location "P" in the Homer Harbor (Figure 6), computed for the eastern landslide at mean high water. At this place tsunami overtopped the
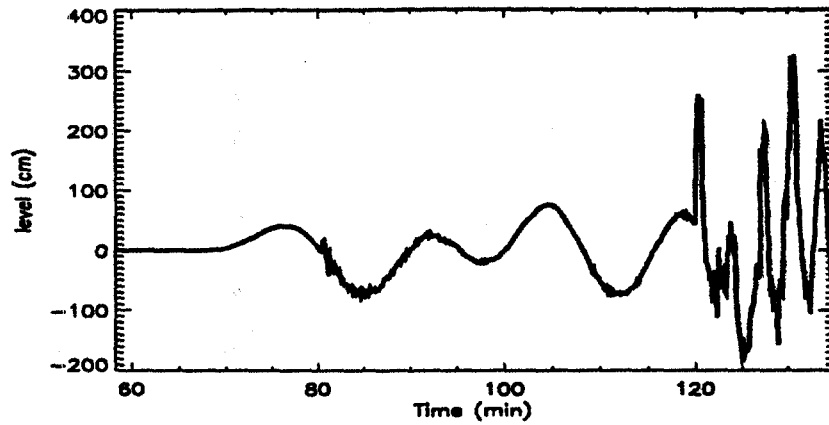
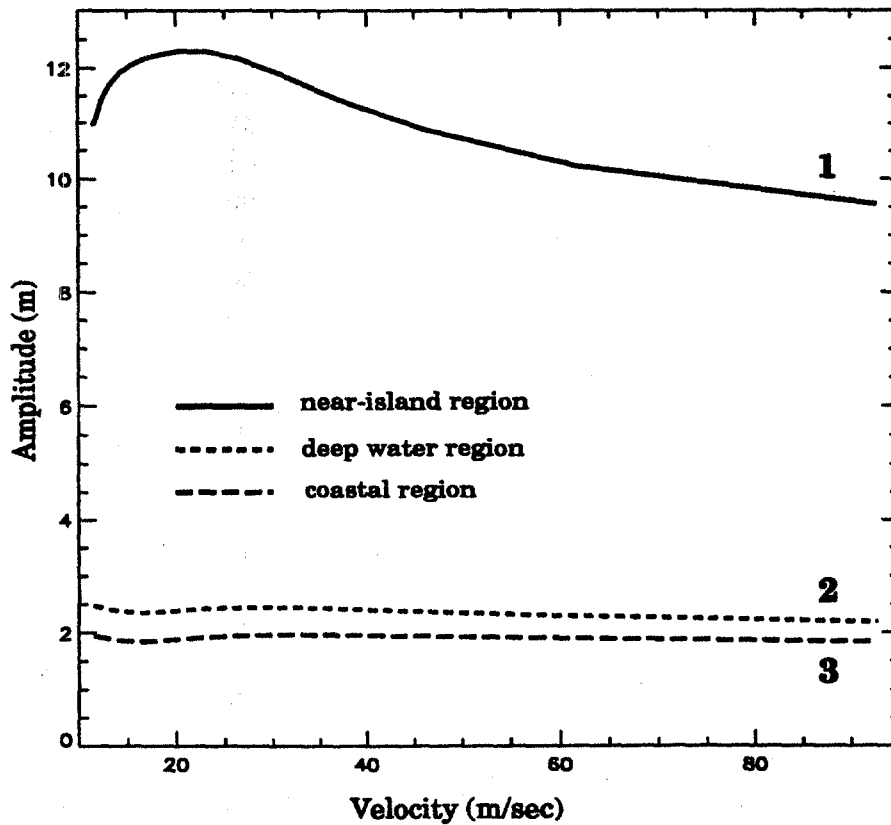Figure 8. Sea level in the Homer harbor for location "P" shown in Figure 6.

Figure 9. Amplitude of the tsunami as a function of the landslide velocity for three different locations on the wave propagation path: 1) in the near-island region; 2) in the deep water region; 3) in the coastal region.

northern shore of the harbor. The short-wave oscillations observed in the plot represent the harbor seiches which are superimposed on long tsunami waves of 25 min period. The figure shows the amplification of the wave signal at time $t = 120$ min. The amplification is due to the energy flow from the main tsunami wave to the short period harbor oscillations. The period of the harbor oscillations can be estimated from horizontal and vertical dimensions of the harbor. The length of the harbor is $L \simeq 500$ m, the average depth is $h \simeq 6$ m. The water depth divided by the length of the harbor is less than 0.1, therefore waves in the harbor can be considered to behave as shallow water waves, and the period of seiche oscillations is determined by the length of the basin and the water depth:

$$T = \frac{2L}{\sqrt{gh}} \simeq 2.1 \; min \tag{7}$$

VI. DISCUSSION AND CONCLUSIONS.

Rigid bottom deformation, conservation of the landslide volume and continuity of the movement between the landslide and the fluid are important assumptions for the theories of the wave generation by a landslide. As LeBlond and Jones (1995) pointed out, these assumptions probably generate an overestimated source function. Typically, a landslide is composed of unconsolidated sediments which move downslope and are accumulated at a new location. The interaction of the unconsolidated sediments is not always a volume conserving process.

Wiegel's (1955) experiments also show that the waves produced by sliding deformable material are smaller than those produced by undeformable materials. Therefore, the calculations performed in this study, which take instantaneous uplifts of the sea floor for initial conditions, must be upper bounds on the size of the tsunami waves generated by an Augustine landslide source.

The presently used Augustine source model is limited by the use of vertically integrated shallow-water equations which cannot model the vertical component of the landslide motion when it enters the sea. More parameters of the landslide have to be considered to adequately model the tsunami generation, and a more sophisticated physical model must be developed for this process. However, some source parameters that have a strong influence on the wave field can be considered within a shallow water model.

The dependence of the tsunami wave amplitude on the velocity-time history of the landslide, $V(t)$, is studied at three points: in the shallow water near Augustine Island about 6 km from the island (the generation phase of tsunami evolution), in the middle region of Cook Inlet (the propagation phase) and close to English Bay (the runup phase). The strongest amplitude dependence on the landslide velocity occurs at the near-source region (Figure 9). The most effective transfer of energy from the moving landslide to the water takes place when the landslide velocity matches the long wave propagation velocity. In the vicinity of Augustine Island, where the water depth is about 50 meters, the strongest tsunami amplitude is generated by a landslide velocity of 20 m/s. In the far field (distance greater than 20 km from St. Augustine), wave amplitude is practically unaffected by the velocity-time history of the landslide. Because the advance of the avalanche along the sea

floor is simulated as a progressive bottom uplift propagating into the open sea, the initial wave height is equal to the thickness of the landslide. A strong correlation is obtained between the height of the landslide and the runup amplitude, which seems to be reasonable for the source model used in this numerical study.

Runup heights at English Bay are calculated for different conditions including the conditions of the 1883 event (northern impact, low tide). Historical records give several values for the wave height at English Bay: 6.1 m (Alaska Commercial Company Records, 1883), 7.6 m and 9.1 m (Davidson, 1884). It is known that the spit separating the English Bay lagoon from Cook Inlet was not flooded in 1883, because no flooding of the spit was reported in the Alaska Commercial Company Records. However, the spit would have been flooded if the 1883 tsunami had occurred at high tide (Davidson, 1884). The computed runup heights at the English Bay spit are 3 m for low tide and 7.4 m for high tide (with respect to the mean low water level); the tidal range is 4.4 m. Because the highest elevation of the spit is about 7 meters, with respect to mean low water level, the runup occurring at high tide causes the spit to be flooded. The results of the runup computations confirm the historic observations rather well, suggesting that the numerical model presented here describes the runup process adequately.

Runup calculations performed for the Homer Spit show that there is some risk for local flooding around the harbor only when the tsunami wave originating at Augustine Island arrives at high tide. It is found that the interaction of the tsunami wave with natural harbor oscillations resulted in amplification of the wave inside the harbor, causing the small area around the harbor to be flooded.

The numerical model for volcanigenic tsunamis in Cook Inlet presented here can be applied easily to any coastal region near a volcano where a tsunami hazard exists, to help provide an effective warning system. However, future research is needed to create better physical and numerical models for the process of tsunami generation by landslides of volcanic origin.

ACKNOWLEDGMENTS

REFERENCES

Aida, I. 1969. Numerical experiments for tsunamis caused by moving deformations of the sea bottom. *Bull. Earthq. Res. Inst. Tokyo Univ.*, **47**(1): 849–862.

Alaska Commercial Company Records. 1883. Log book. *University of Alaska Archives, Fairbanks.*

Begét, J.E. and J. Kienle. 1992. Cyclic formation of debris avalanches at Mt. St. Augustine. *Nature*, **356**: 701–704.

Begét, J.E. and C.J. Nye. 1994. Postglacial eruption history of Redoubt volcano, Alaska. *J. of Volc. and Geotherm. Res.*, **62**: 31–54.

Davidson, G. 1884. Notes on the volcanic eruption of Mount St. Augustine, Alaska, Oct. 6, 1883. *Science*, **3**: 186–189.

Flather, R.A. and N.S. Heaps. 1975. Tidal computations for Morecambe Bay. *Geophys. J. Roy. Astr. Soc.*, **42**, 489–517.

Imamura, F. and M. Imteaz. 1995. Long waves in two layers: governing equations and numerical model. *Science of Tsunami Hazard*, **11**(1): 3–24.

Kajiura, K. 1963. The leading wave of tsunami. *Bull. Earthq. Res. Inst. Tokyo Univ.*, **41**(3): 535–571.

Kienle, J., Z. Kowalik and T.S. Murty. 1987. Tsunami generated by eruptions from Mount St. Augustine Volcano, Alaska. *Science*, **356**: 1442–1447.

Kowalik, Z. and T.S. Murty. 1993. *Numerical Modeling of Ocean Dynamics.* Advanced Series on Ocean Engineering, Volume 5. World Scientific Publ., 481 pp.

Lander, J. F. and P. A. Lockridge. 1989. *United States Tsunamis.* National Geoph. Data Center. Boulder, 265 pp.

LeBlond, P.H. and A.T. Jones. 1995. Underwater landslides ineffective at tsunami generation. *Science of Tsunami Hazard*, **11**(1): 25–26.

Mader, L.Ch. 1988. *Numerical modeling of water waves.* Berkeley: University of California Press.

Noda, E. 1970. Water waves generated by landslides. *J. of Waterways, Harbors and Coastal Engineering Division*, Proc. Am. Soc. Siv. Eng., **WW4**: 835–853.

Reid, R.O. and R.O. Bodine. 1968. Numerical model for storm surges in Galveston Bay. *J. Waterway Harbour Div.*, **94**(**WWI**), 33–57.

Sielecki, A. and M.G. Wurtele, 1970. The numerical integration of the nonlinear shallow-water equations with sloping boundaries. *J. Comput. Physics*, **6**: 219–236.

Troshina, E.N. Tsunami waves generated by Mt. St. Augustine Volcano, Alaska. *M.S. thesis*, 84 pp., University of Alaska Fairbanks, 1996.

Wiegel, R.L. 1955. Laboratory studies of gravity waves generated by the movement of a submerged body. *EOS*, **36**: 759–774.

SCIENCE OF
TSUNAMI HAZARDS

PUBLICATION FORMAT INFORMATION

Typing area is 25 by 19 cm.

One-column text.

All text to be single-space.

Indent 5 spaces to start a new paragraph.

Page numbers in lower right hand corner in blue pencil.

Top half of first page to contain title in CAPTIALS,
   followed by authors and author affiliation centered on page.

Bottom half of first page to contain abstract with
   heading ABSTRACT centered on page.

Send original camera ready paper and a copy to

Dr. Charles Mader, Editor
Science of Tsunami Hazards
Mader Consulting Co.
1049 Kamehame Drive
Honolulu, Hawaii 96825-2860, USA

APPLICATION FOR MEMBERSHIP

THE TSUNAMI SOCIETY
P. O. Box 25218
Honolulu, Hawaii 96825, USA

I desire admission into the Tsunami Society as: (Check appropriate box.)

☐ Student   ☐ Member   ☐ Institutional Member

Name _____Signature _____

Address _____Phone No. _____

_____

Zip Code _____Country _____

Employed by _____

Address _____

Title of your position _____

FEE: Student $5.00   Member $25.00   Institution $100.00

Fee includes a subscription to the society journal: SCIENCE OF TSUNAMI HAZARDS.

Send dues for one year with application. Membership shall date from 1 January of the year in which the applicant joins. Membership of an applicant applying on or after October 1 will begin with 1 January of the succeeding calendar year and his first dues payment will be applied to that year.